Rotation Measures in Galaxy Clusters from Background and Embedded Sources: Estimating the Cluster Magnetic Fields

A THESIS
SUBMITTED TO THE FACULTY OF THE GRADUATE SCHOOL
OF THE UNIVERSITY OF MINNESOTA
BY

Andrew Richard Johnson

IN PARTIAL FULFILLMENT OF THE REQUIREMENTS
FOR THE DEGREE OF
Master of Science

Thomas W. Jones, Advisor

June, 2014

Acknowledgements

There are many people that I would like to thank for allowing my graduate career and this thesis to come together. They have provided me the strength and perseverance to see through to the culmination of my graduate education. Without all of their support and guidance, none of this would have been possible.

I would first like to thank my family, who have provided me the love and support to make all of this come together. My wife, Jacie, has stood by me through all the good and the bad, the triumphs and the stresses. I can not express enough how much I have appreciated having her by my side through this entire process. To my two daughters, Ashlyn and Andi, who have explored my education as I have progressed through it, all while developing a passion for physics and astronomy with their dad. To my son, Avery, whose energy and curiosity is a constant reminder to how my journey got started. To my parents for their nurturing and being the constant force of positivity that I have needed to be successful.

I would like to strongly thank both my advisor, Tom Jones, as well as Larry Rudnick for guiding me through my graduate career. They have helped me develope my skills in critical thinking, scientific reasoning, and showed me how to see the world from a different perspective all which I will forever use and cherish. Both their patience and their constant strive to challenge me have allowed me to grow as an analytical thinker. Without their support, encouragement, and the occasional slight nudge when I may have veered off course, none of this would be possible.

I thank all of the graduate students, faculty and staff of the Minnesota Institute for Astrophysics. In particular, I am forever grateful to Peter Mendygral, Jennifer Delgado, and Paul Edmon. They provided me the skills and encouragement that were necessary to make this thesis come together. To Dinesh Shenoy, who was and is a great friend

Dedication

To my loving wife, Jacie, my three wonderful children, Ashlyn, Andi, and Avery.

Abstract

Rotation measures (RMs), derived using polarized radio sources embedded in clusters, are commonly used to estimate magnetic field strengths in intra-cluster media (ICMs). To obtain these field values, assumptions are often invoked that involve: no RM contributions from the RM source, adequate sampling of the cluster ICM, and power law distributions of the magnetic power spectra. We explore the impact of such assumptions using synthetic RM measurements of the ICM of a dynamical cluster extracted from a magneto-hydrodynamic (MHD) cosmological simulation. We first explore the viability of estimating cluster magnetic fields using both RMs fully sampling the cluster as well as limited sampling using non-interacting RM sources placed within the cluster. We then evolve the cluster both with and without an interacting central active galactic nucleus (AGN) to examine how a radio source interacting with the surrounding ICM modifies the observed RMs. We applying a density dependent RM coherence length to our models and find that the magnetic field estimates are improved over models with a constant RM coherence length. We also suggest that a magnetic field model only need be characterized by a coherence length, the central dispersion value, and the scaling with density to effectively produce observed cluster RMs. However, uncertainties– predominantly due to large scale anisotropies– produce errors in the estimates of cluster magnetic fields that under ideal conditions are a factor of 50%. For sources that interact with the surrounding ICM, we find that the motions induced in the local ICM do not significantly alter the overall distribution of RMs observed in a "foreground screen". However, if the magnetic fields introduced by the radio source are sufficiently strong, non-negligible RM contributions attributed to ICM entrainment with the radio source plasma could contaminate RM observations making estimates of the undisturbed ICM magnetic fields perilous.

Contents

List of Tables

List of Figures

Chapter 1

Introduction

- Chapter 2 provides an overview of the history and science leading behind rotation measure analyses of magnetic fields in galaxy clusters.

- Chapter 3 describes the numerical set up of the cluster used in our analyses. We further describe the physical properties of this cluster placing emphasis on how to characterize the tangled magnetic fields that are present.

- Chapter 4 gives an analysis of estimating cluster fields from both idealized and non-idealized rotation measure sources in a cluster. All sources are treated as passive– not interacting with the surrounding cluster. We then determine the inherent uncertainties present in any magnetic field estimates determined using the current rotation measure paradigm.

- Chapter 5 explores a rotation measure analysis of the magnetic fields using a jet from an active galactic nucleus placed at cluster center. The outflow from this jet modifies the ambient cluster. We determined how this modification influences and alters the rotation measures obtained from the interacting source.

- Chapter 6 provides conclusions based on the results outlined in the previous chapters.

Chapter 2

Background

The ICM of galaxy clusters is magnetized as indicated by the presence of large scale synchrotron radio halos present in some clusters, as well as the observed Faraday rotation of polarized radio emission traversing the cluster. The origin and structure of these fields are actively under debate, although the ICM and embedded magnetic fields are widely believed to be turbulent (e.g., Schuecker *et al.*, 2004; Sanders *et al.*, 2011). Enhanced knowledge of these fields allows deeper understanding of their role in cluster dynamics and thermodynamics. The strength and structure of magnetic fields control the scale and isotropy of transport processes such as viscosity and thermal conduction. For instance, magnetic field and associated transport anisotropies can stabilize structures such as cold fronts (e.g., Zuhone *et al.*, 2010) or lead to instabilities that could influence cluster thermal structure (e.g., Parrish *et al.*, 2012). Furthermore, kinetic turbulence revealed by the field structure and to a lesser extent the field itself could provide a means of non-thermal pressure support and contribute to the overall energy budget of a cluster (e.g., Dolag *et al.*, 2008).

Linearly polarized radio synchrotron emission propagating through a magnetized ICM plasma is subjected to Faraday rotation. The angle of the rotation scales as $\lambda^2 \times$RM, where

$$RM = 812 \int_0^L n_e B_\parallel \, \mathrm{d}l, \qquad (2.1)$$

and n_e is in units of cm^{-3}, $B_\parallel$ is in units of μG, dl is in units of kpc, and RM is in units

of $\mathrm{rad\,m^{-2}}$. Measured RMs can serve as an observational tool to probe cluster magnetic fields (see Carilli & Taylor (2002)). The electron density can be obtained from X-ray measurements of the thermal emitting plasma, while the effective characteristic path length is typically on the order of the size of the cluster core. That information along with Eqn. 2.1 provide a measure of the mean parallel component of the magnetic field along a given line of sight. Since the magnetic field is not uniform, but tangled, some effort is required to obtain meaningful estimates of the local field strength from ICM RM measurements.

By invoking assumptions such as an isotropic, randomly tangled field over a uniform scale length, Eqn. 2.1 applied to an ensemble of RM values gives estimates of the overall strengths of the ICM fields. In particular Eqn. 2.1 can be modified under these circumstances to express the RM standard deviation in terms of correlated patches of size, Λ, approximately as,

$$\sigma_{RM} = 812\,\bar{n}_e \sigma_{B,\|}\,\Lambda\,\sqrt{\frac{L}{\Lambda}} \qquad (2.2)$$

where the units are the same as Eqn. 2.1. Here σ_{RM} is the RM dispersion and is sensitive to $\sigma_{B,\|}$, the dispersion in the parallel component of the magnetic field. The RM coherence length, Λ, will be related to the coherence length of the magnetic field and L represents the path length that the polarized emission traverses through the cluster. As Eqn. 2.2 is sensitive to dispersions in the magnetic field, it will not be sensitive to any large scale ordered components of the field. Furthermore, effective use of this RM model requires that multiple lines of sight are sampled, and these samples cover independent coherent RM patches.

Observational efforts to measure cluster magnetic fields using RM distributions have been extensive, using RMs measured from both extended radio emitting synchrotron sources as well as multiple point sources in galaxy clusters. Often, multiple embedded radio sources have been used to estimate magnetic fields, such as efforts made in Abell 119 (Feretti *et al.*, 1999) and the Coma cluster (Bonafede *et al.*, 2010). Likewise, large cluster-centric AGNs such as those in Hydra (Taylor & Perley, 1993), Perseus (Taylor *et al.*, 2006), Abell 400 & Abell 2634 (Eilek & Owen, 2002), and Abell 2199 (Vacca *et al.*, 2012) have made nice targets for RM analyses of clusters. These measurements

suggest maximum magnetic field strengths at cluster centers on the order of 1-15 μG with strengths steadily decreasing further out in the cluster. Xu *et al.* (2012) have created numerical, MHD simulations of clusters and shown that the magnetic field results obtained observationally are consistent with the above interpretation of typical observed RMs.

However, it has been argued that using sources embedded within the cluster will not provide a true probe of the foreground magnetic fields of the ICM. This was first put forward by Rudnick & Blundell (2003) who suggested that RMs originating from embedded sources could contain contamination originating from the source itself. Any such contamination from the source would need to be disentangled in order to extract the information contained in the foreground ICM fields. Enßlin & Vogt (2003b) rebutted this argument by analyzing patterns comparing the RMs and initial polarization angles of the emission, concluding a lack of strong correlation between the two suggests RM contribution from the source is negligible. On the other hand, the issue has arisen again with recent observations of banded structures in the RM distributions of extended sources (Guidetti *et al.*, 2011) that have been attributed to compression and draping of the local ICM fields around the radio lobes. Also, there has been evidence of anomalous, asymmetric RM features in extended source RMs (Guidetti *et al.*, 2012).

Chapter 3

Numerical Properties of Simulated Cluster

3.1   Numerical Set-up

The ICM that supplied the basis of our synthetic RM observations was the same one used by Mendygral et $al.$ (2012). It came from the 1.5×10^{14} M$_\odot$ cluster $g676$ (Dolag et $al.$, 2009) extracted at a redshift of $z \approx 0$ from a very high resolution cosmology simulation ($h = 0.7$, $\Omega_M = 0.3$, and $\Omega_\Lambda = 0.7$) carried out with an MHD implementation of the SPH GADGET-3 code (Dolag & Stasyszn, 2009). We mapped the cluster onto a Cartesian grid of uniform resolution with $\Delta x = \Delta y = \Delta z = 1$ kpc. Details of the $g676$ cluster and the simulation that produced it can be found in Mendygral et $al.$ (2012) and references therein. This cluster was chosen for its lack of recent mergers (the last major merger occurred 7 Gyr prior to our simulations' initial conditions). Despite its relatively relaxed morphology, the $g676$ ICM still contains significant dynamical motions; i.e., large scale cluster "weather" associated with "sloshing" motions with velocities approaching the cluster sound speed. The core of the extracted cluster has a radius $r_c \approx 50$ kpc, central density, $\rho \sim 10^{-25}$ g cm^{-3} and a temperature, $T \approx$ 1.6 keV. The associated cluster core sound speed is $c_s \approx 650$ km s^{-1}. The azimuthally averaged density at 500 kpc was $\rho(r = 500 \text{ kpc}) \sim 3\text{x}10^{-28}$g cm^{-3}. The $g676$ ICM is turbulent (Zhuravleva et $al.$, 2011). Core turbulent velocities are ~ 50 km s^{-1}, so the core turbulent pressure iss $< 1\%$ of the total pressure. Outside the core turbulent velocities increase to ~ 100 km s^{-1}, but

still contribute $< 5\%$ of the total pressure. The cluster magnetic field has central values, $B_0 \sim 2 - 3\mu G$, that developed from a primordial field with strength $10^{-11}\mu G$. Field strengths decrease by an order of magnitude at distances 500 kpc from cluster center. Without accounting for a tangled magnetic field, from Eqn. 2.1 we would anticipate RM $\sim 600\, rad\, m^{-2}$ for lines of sight through the cluster center, falling off to RM $\sim 1\, rad\, m^{-2}$ for projected radial distances 500 kpc from the center.

3.2 Density Distribution

Figure 3.1 displays the projected gas (electron) density distribution for the *g676* cluster as viewed along one of the three principal axes of our grid. Clusters emit X-rays from thermal bremsstrahlung emission. Observationally, this gives us a tracer of the projected n_e^2 distribution in the cluster. Figures 5 and 6 in Mendygral *et al.* (2012) illustrate the structure and thermal X-ray appearance of the *g676* cluster. As evident in both the gas and X-ray distributions, spherical asymmetries in the density are present in our cluster. We can still attempt to model the density by assuming an azimuthal symmetry when taking radial averages for the density distribution. The deviations from this assumption will contribute to errors when using RMs to estimate the cluster magnetic fields.

It is conventional to model ICM electron distributions using beta law profiles (Cavaliere & Fusco-Femiano, 1976),

$$n_e(r) = \frac{n_{e,0}}{(1 + (\frac{r}{r_c})^2)^{\frac{3}{2}\beta_c}}, \tag{3.1}$$

where $n_{e,0}$ is the central electron density, r_c is the core radius of the cluster, and β_c represents the ratio of galaxy to the gas velocity dispersions in a nominally assumed spherically symmetric, isothermal cluster. Furthermore, if we use the square of the electron density, n_e^2, as a proxy for the thermal bremsstrahlung emission observed X-ray observed in clusters, we can fit an azimuthally symmetric surface density-squared, $\Sigma_{n_e^2}$, as a function of projected distance, a, by

$$\Sigma_{n_e^2}(a) = \frac{\int_{a=0} n_e^2 \, \mathrm{d}\, z}{(1 + (\frac{a}{r_c})^2)^{3\beta_c + \frac{1}{2}}} \tag{3.2}$$

where d z is the path along the line of sight.

We display in Figure 3.2 the profile of $n_e(r)$, using azimuthal averages of the density within the 3D grid, fit using Eqn. 3.1. The fits provide a core radius, $r_c = 41$ kpc, and $\beta_c = 0.75$, which are well within the range of observed galaxy cluster surveys (e.g. Vikhlinin *et al.* (2006)). Also shown are radial profiles of the projected electron density-squared distribution (also azimuthally averaged) along the three principle axes of the simulation grid. There are errors in our fit to Eqn. 3.2 by as much 15% near cluster center and less than 5% when looking at projected distances beyond a core radius. These errors are a result of the large scale anisotropies present within the cluster and reflect the deviations from our assumption of azimuthal symmetry.

3.3 3D Magnetic Field Distribution

A view of the projected $|\vec{B}|$ can be viewed in Figure 3.1. From Eqn. 2.2, we see that the appropriate measure of the magnetic field is the dispersion about the component parallel to the line of sight, $\sigma_{B,\parallel}$. If the field is assumed to be isotropic, we can relate the dispersion of the parallel component of the field to the total field dispersion by $\sigma_{B,\parallel} = \frac{\sigma_B}{\sqrt{3}}$. Also, an isotropic field should have $\langle \vec{B} \rangle = 0$. So, the validity of an isotropic field distribution can be shown for $\langle \vec{B} \rangle \ll \sigma_B$.

Observationally, the cluster distribution of σ_B is not known and thus must be modeled. A field with magnitude scaling with the density is theoretically motivated, with a frozen in field scaling with density as $n^{\frac{2}{3}}$ and a field amplified by the turbulent dynamo scaling as $n^{\frac{1}{2}}$ (Schekochihin & Cowley *et al.*, 2004). Simulations of MHD cluster formation further motivate this by showing a strong scaling of the magnetic field with the cluster density (e.g., Dolag *et al.*, 2005). Thus it is convenient to assume a field that scales with the density distribution as the cluster density distribution is often well constrained by the thermal X-ray emission. We will more generally assume a magnetic field that scales with electron density by $\sigma_B \sim n_e^{\eta}$, where η is not known a priori. If we assume the orthogonal components of the magnetic field are uncorrelated, we can express $\sigma_B = \sqrt{\langle \vec{B}^2 \rangle - \langle \vec{B} \cdot \vec{B} \rangle}$ with σ_B being calculated over some volume. To determine the actual η value for our cluster cluster, we calculate $\langle n_e \rangle$ and σ_B within volumes defined by shells of uniform thickness with uniform logarithmic spacing. We then use

a least squares fit to obtain the proportionality between σ_B and $\langle n_e \rangle$. The results are shown in Figure 3.2 and give us values of $\sigma_{B,0} = 1.9$ and $\eta = 0.5$.

Using the scaling of the magnetic field dispersion with the density, we can express the magnetic field dispersion as a function of radius by

$$\sigma_B(r) = \frac{\sigma_{B,0}}{(1 + (\frac{r}{r_c})^2)^{\frac{3}{2}\eta\beta}} \tag{3.3}$$

where β and r_c are obtained from the electron density distribution. By performing least squares fits of $\sigma_{B,0}$ and η using σ_B as a function of shell radius, we find that the central value of the magnetic field dispersion is $\sigma_{B,0} = 1.9\mu G$, consistent with the result above. The radial profile of the magnetic field for our cluster is shown in Figure 3.2.

The magnetic field in the *g676* cluster is tangled and a description of some coherent scale must be formulated to apply Eq. 2.2 to an RM analysis. Figure 3.3 displays power spectra over our full simulation box (so a 1 Mpc^3 volume) for both the magnetic and kinetic energy. The spectra are consistent with results derived from other MHD cluster formation simulations (e.g., Xu *et al.*, 2011). No correction was made for large scale weather, so those motions are included in the power spectrum and supply a significant portion of the kinetic energy power on the largest scales. In contrast, the large scale power in the magnetic field as a result from these motions is small compared to the total magnetic energy power. The magnetic field power spectra are also in reasonable agreement with ideal and non-ideal MHD simulations designed to follow the growth of initially weak magnetic fields in subsonic turbulence (e.g., Cho *et al.*, 2009; Jones *et al.*, 2011).

The total energy found by integrating the kinetic energy power spectrum is about 5×10^{60} erg, so about 8% of the ICM thermal energy. The integrated magnetic energy found from the magnetic power spectrum in Figure 3.3 is about 2.4×10^{58} erg, which is only about 0.5% of the kinetic energy revealed in that power spectrum and less than 0.04% of the total thermal energy. Evidently the turbulence has not, at least globally, approached a saturated state in which kinetic and magnetic turbulent energies would be in rough equipartition. The power spectra reflect that. The kinetic energy power spectrum is roughly consistent with the classical Kolmogorov form, $P(k) \propto k^{-5/3}$ over much of its range; the magnetic power spectrum is not. The essential physical difference

is that unlike turbulent motions in the inertial range, the magnetic field does not develop directly through a cascade of energy from large to small scales. Rather, the field is amplified by the so called "fluctuation dynamo", which comes from field lines being stretched by fluctuations in the velocity field. In a turbulent flow those fluctuations are most rapid on small scales somewhat above the viscous dissipation scales, so the magnetic field energy develops first on small scales (e.g., Schekochihin & Cowley *et al.*, 2004). The resulting magnetic field power spectrum is very broadly peaked on scales that only approach the turbulent driving scale over many large-scale eddy times (Cho *et al.*, 2009).

Application of Eqn. 2.2 to estimate the cluster fields requires that some correlation length to the field, Λ be known. As the field structure in *g676* is readily available to us, we are able to obtain estimates of Λ. The magnetic power spectrum in Figure 3.3 peaks gradually over $k \sim 10 - 20$ Mpc^{-1}, so on scales $\sim 50 - 100$ kpc. Characteristic scales for the magnetic field should lie roughly in this range. One quantitative measure of the scale of the magnetic field turbulence that has been suggested for comparison with RM correlation scales (Cho & Ryu, 2009) is the so-called integral length, L_{int}, defined in terms of the power spectrum as,

$$\mathrm{L_{int}} = \frac{\int E_B(k)/k \, \mathrm{d}k}{\int E_B(k)\mathrm{d}k}. \tag{3.4}$$

Using Eqn. 3.4 we obtain $\mathrm{L_{int}} \approx 54$ kpc for the magnetic field in our full simulation volume (Figure 3.3). We have computed nine additional magnetic field power spectra for cluster-centered volumes ranging in size from 100 - 900 kpc. From these we find L_{int} increasing smoothly from $L_{int} \approx 20$ kpc in the core to the $L_{int} \approx 54$ kpc already mentioned for the full simulation box.

Comparing each of these L_{int} to the mean plasma densities of the volumes over which the associated magnetic field power spectra were computed we find a tight correlation consistent with $L_{int} \propto \langle n_e \rangle^{-1/4}$. These scaling behaviors suggest that much of the global distribution of magnetic field properties within the cluster is dominated by compression. Recall the familiar result from flux conservation that the strength of a tangled magnetic field in an ideal conducting medium would scale as $B \propto n_e^{2/3}$ in response to isotropic compression, while the characteristic lengths of field line segments

would scale as $\Lambda \propto n_e^{1/3}$. The presence of dynamo action and or field line slippage would weaken the power of the scalings, so scalings that approximate $B \propto n_e^{1/2}$ and $\Lambda \propto n_e^{1/4}$ represent reasonable expected behaviors in an ICM. Thus, an appropriate assumption would be that the field coherence length would scale with density as $\Lambda \propto n_e^{1/2\eta}$.

3.4 Figures
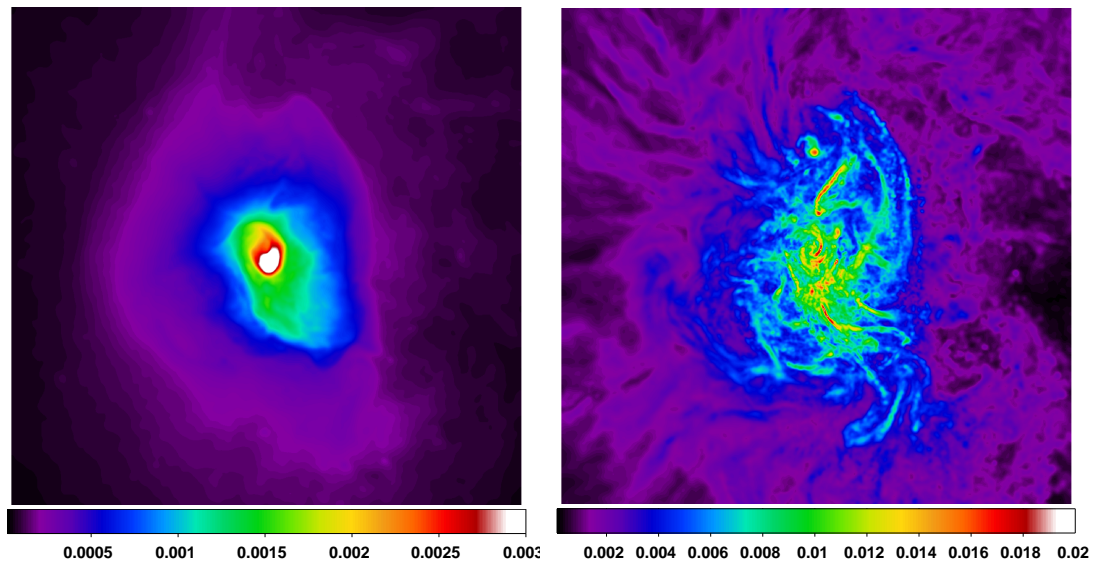
Figure 3.1 Maps of the projected log-electron number density along the z-axis (left), and projected magnitude of the magnetic field (right). The linear scale is equal among the two images with the entire length of a box being 1 Mpc.
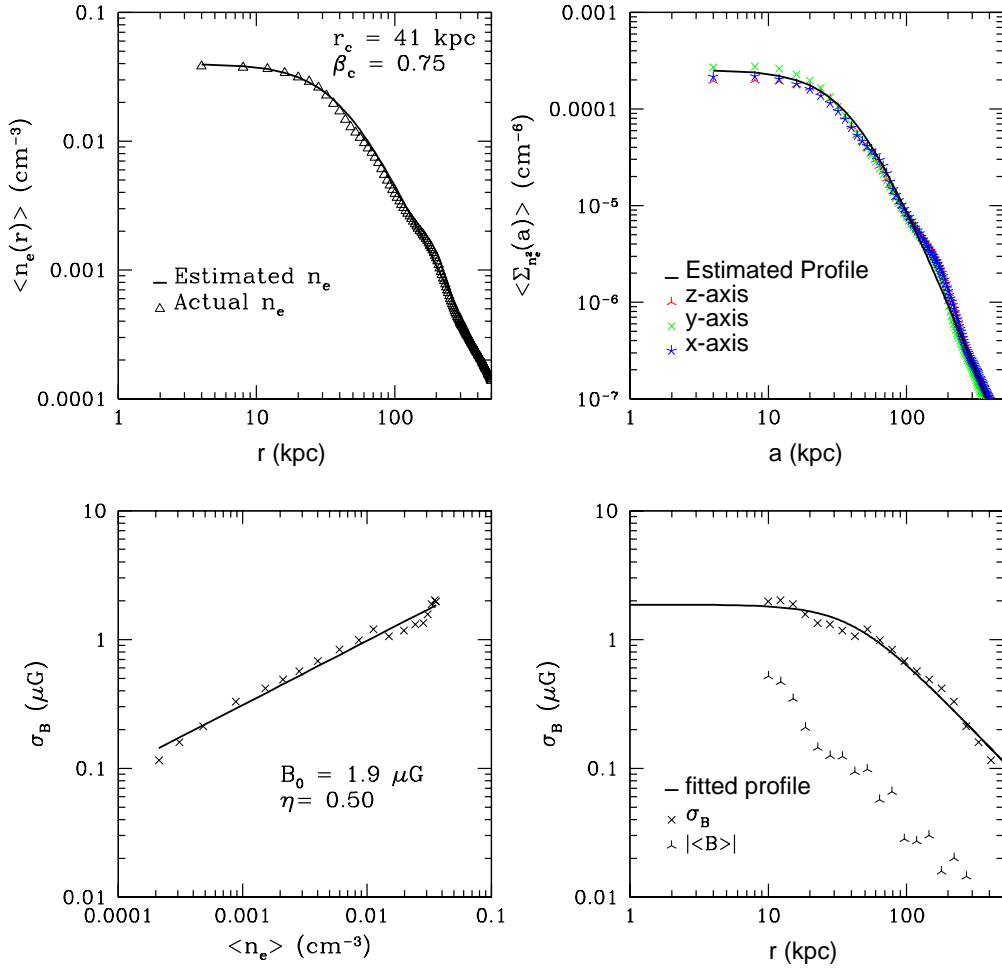
Figure 3.2 Global cluster properties (azimuthally averaged) including: the mean electron density with β-profile fit by Eqn 3.1 (upper left), the average projected number density square with β-profile fit by Eqn 3.2 (upper right), the dispersion in the magnetic field, σ_B, versus the averaged 3D density along with a fit for $\sigma_B \sim n_e^\eta$ (lower left), and σ_B as a function of radius fit using Eqn. 3.3 as well as $|\langle B \rangle|$ (lower right).
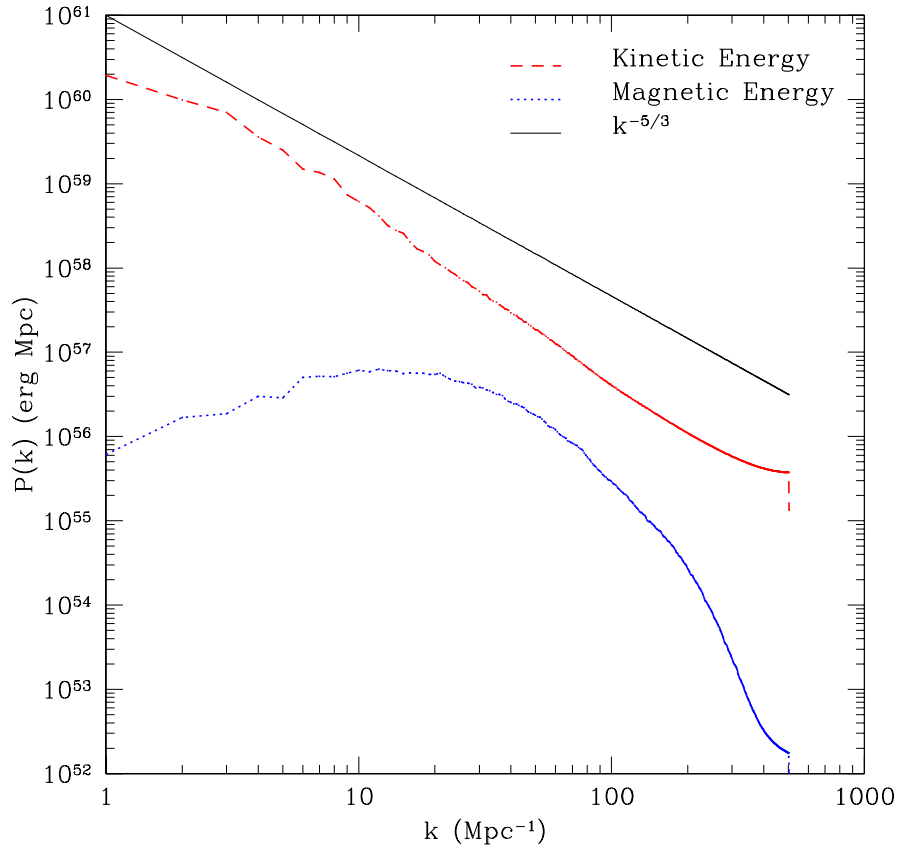
Figure 3.3 Power Spectrum of the kinetic energy and magnetic energy of the *g676* ICM inside the 1 Mpc^3 simulation box. Also included is a line representing a Kolmogorov type (k$^{-5/3}$) spectrum. Of particular note is the broad turnover of the magnetic power spectrum for k $\sim 8 - 20$ Mpc^{-1}, so on scales k $\sim 50 - 120$ kpc.

Chapter 4

Non-Interacting Radio Source Analysis

Traditionally, when observationally estimating magnetic fields from RMs in clusters, simple models of a turbulent magnetic field are often assumed. The magnetic field is typically assumed to be Gaussian and to have a power spectrum that follows a power law to some maximal scale (e.g., Murgia *et al.*, 2004; Laing *et al.*, 2011). If an outer RM scale is assumed or measured, Monte-Carlo simulations, for example, can be performed to constrain the power law index of the magnetic field power spectrum and central field strength by comparing the simulated RMs to the observed RM distributions in the cluster. However, as stated in Section 2.3, simulations and theory do not typically support power law forms for the magnetic field power spectra in clusters. Nominally, the only properties of the cluster needed to extract magnetic field information are some assumed RM distribution in the cluster and a characteristic scale of the magnetic field fluctuations. Given those assumptions, we suggest a prescription for estimating the magnetic field inferred directly from measurables in the cluster.

Any realistic RM analysis of a cluster must deal with cluster-scale inhomogeneities, beginning with basic radial dependencies of density and magnetic fields (e.g., Kunz *et al.*, 2011). Thus, *both* Λ and L will then be functions of position in the cluster, and must be treated as such when extracting the magnetic field from the RM distributions. In addition, complex and ongoing dynamical processes are likely to introduce significant

asymmetries to these structures. The simulated cluster, *g676*, that we analyze here provides a convenient context to explore our ability to extract reliable magnetic field information from RM distributions in cluster environments. Recall that the *g676* ICM contained turbulent motions and large scale, bulk "weather" that will be represented in the RM distribution. Both of these are likely to be present in actual ICMs, even when they are not actively engaged in major mergers.

4.1 Magnetic Field Model From σ_{RM}

We express the RM dispersion as a function of projected radius by integrating Eqn. 2.1 along the entire line of sight and combining with Eqn. 2.2 (see Felten (1996)) we obtain

$$\sigma_{RM}(a) = \frac{\sigma_{RM,0}}{(1 + (\frac{a}{r_c})^2)^\alpha} \tag{4.1}$$

with $\sigma_{RM}(a) = \sqrt{\langle RM^2 \rangle - \langle RM \rangle^2}$ being calculated in an area about some projected radius a, and where we have defined

$$\sigma_{RM,0} = \frac{812 \, \pi^{1/4}}{\sqrt{3}} \, n_0 \sigma_{B,0} \, \Lambda_0^{1/2} \, r_c^{1/2} \sqrt{\frac{\Gamma(2\alpha)}{\Gamma(2\alpha + \frac{1}{2})}} \tag{4.2}$$

and we have assumed an isotropic distribution of the magnetic field so $\sigma_{B,||} = \frac{\sigma_B}{\sqrt{3}}$. We have also introduced a parameter, α, which will not only depend on the β_c value from the density distribution, but also the density scaling parameters of both the magnetic field and RM coherence length. In equation Eqn. 4.2, the 0 subscripts correspond to values measured at cluster center. Rearranging Eqn. 4.2, we can express

$$\sigma_{B,0} = \frac{\sqrt{3}}{812 \, \pi^{1/4}} \frac{\sigma_{RM,0}}{n_0 \, \Lambda_0^{1/2} \, r_c^{1/2}} \sqrt{\frac{\Gamma(2\alpha + \frac{1}{2})}{\Gamma(2\alpha)}} \tag{4.3}$$

From this, we see that the central value of $\sigma_{B,0}$ can be found in a cluster if $\sigma_{RM,0}$, α, and Λ_0 can be determined.

A direct fit to the observational RM data using Eqn. 4.1 can ideally provide $\sigma_{RM,0}$ and α, if $\sigma_{RM,0}$ and α are free parameters and it is assumed r_c and β_c are well constrained by observational X-ray measurements. From these fits, for a constant coherence length

$\Lambda = \Lambda_0$, then

$$\alpha = \alpha_1 = \frac{3}{2}(1+\eta)\beta_c - \frac{1}{4} \qquad (4.4)$$

As detailed in the previous section, a more appropriate assumption would be that of a density dependent coherence length with $\Lambda = \Lambda_0(\frac{n_e}{n_0})^{-1/2\eta}$. In this scenario, a factor of Λ must be incorporated into the integral, and the resulting value of alpha is

$$\alpha = \alpha_2 = \frac{3}{2}(1+\frac{3}{4}\eta)\beta_c - \frac{1}{4} \qquad (4.5)$$

Thus, we can get two of the three parameers ($\sigma_{RM,0}$ and α) needed directly from the observational RM profiles in the cluster.

4.2   RM Coherence Scale

For clusters fields that develop through turbulent amplification, a relationship between RM coherence length and magnetic field structures in driven MHD turbulence is presented in Cho & Ryu (2009). They showed in particular for saturated turbulence that Λ, defined in the context of Eqn. 2.2 above, should be related to the turbulent magnetic field integral length, L_{int}, as $\Lambda = \frac{3}{4}L_{int}$. We will establish the notation, $\Lambda_{CR} = \frac{3}{4}L_{int}$. Using the magnetic field power spectra in $g676$, Λ_{CR} varies for our cluster, between $\Lambda_{CR} \approx 15$ kpc in the cluster core to $\Lambda_{CR} \approx 40$ over our full volume.

Observationally, Λ_{CR} is not a measurable quantity. However, the RM coherence length can be measured directly through the 2nd order structure function of the RM distribution. The 2nd order RM structure function defined as

$$S(|\Delta\vec{a}|) = \langle | RM(\vec{a}) - RM(\vec{a} + \Delta\vec{a}) |^2 \rangle, \qquad (4.6)$$

where $\Delta\vec{a}$ measures an offset relative to a projected position, or "seed point", with respect to the cluster center, $\vec{a}$, and the averaging is done over all $\vec{a}$ and $\Delta\vec{a}$ such that $|\Delta\vec{a}|$ is some fixed value. The 2nd order structure function is tied to the Power Spectrum in turbulence theory. Specifically, for homogeneous turbulence classified by a power law spectrum characterized by $P(k) \sim k^n$, $S(|\Delta\vec{a}|)$ is also a power law characterized by

slope $-(n+1)$ for $|\Delta\vec{a}|$ that are within the inertial range of the turbulence. When the power spectrum is not power law, the 2nd order structure function will show structure below a scale that is approximately the integral scale. Above this scale, the slope of the 2nd order structure function will nominally go to zero as the field being measured becomes uncorrelated. As the RMs are directly related to the line of sight component of the magnetic field, we would expect structure functions of the RMs to directly relate to the structure functions of the overall magnetic field when isotropy is assumed.

In Figure 4.1 we plot structure functions for RMs integrated through the entire simulation box using viewing angles along the three principal grid axes. Each structure function exhibits a distinct scale where the slope tends towards 0, which we identify as the RM coherence length. Specifically, we select the smallest scale, $|\Delta\vec{a}|$, for which $\frac{d(\ln(S(|\Delta\vec{a}|)))}{d(\ln(|\Delta\vec{a}|))} = 0$. Each of the structure functions in Figure 4.1 satisfy this condition for $|\Delta\vec{a}|$ in the range 20 - 30 kpc. That lies between the $\Lambda_{CR} \approx 15$ kpc estimated for the cluster core and $\Lambda_{CR} \approx 40$ kpc estimated for the full box. As the 2nd order structure function can be calculated directly from the observed RMs, we adopt this method of obtaining a reasonable estimate of the RM coherence length. We define the coherence length obtained in this way as Λ_{SF}.

Ultimately, we want the value of the Λ_0, which, for a density dependent Λ will not be the same as the measured Λ_{SF} Λ_{SF} should represent some cluster average Λ and thus we can treat Λ_{SF} as some characteristic Λ that applies at a distance we define r_{eff}. Using this r_{eff} along with the assumed scaling of Λ with density described in section 2.3, allows us to characterize Λ as a function of radius.

The value of r_{eff} should be some weighted average of our RM sources positions within the cluster. To determine this weighting we explore the behavior of the 2nd order structure function used to calculate Λ_{SF}. If we only consider values of $|\Delta a| = \Lambda_{SF}$, then the expansion of only those components of the structure function give

$$\langle (RM(\vec{a}) - RM(\vec{a} + \vec{\Lambda}_{SF}))^2 \rangle = \langle RM^2(\vec{a}) \rangle + \langle RM^2(\vec{a} + \vec{\Lambda}_{SF}) \rangle - 2\langle RM(\vec{a})RM(\vec{a} + \vec{\Lambda}_{SF}) \rangle$$

$$(4.7)$$

For an isotropic field, $\langle RM^2(\vec{a}) \rangle$ is just the average of $\sigma_{RM}(a)$ over all a weighted by the number of points at each a.

As Λ_{SF} represents the scale where the RMs become uncorrelated, the second term is expected to be equal to the first term. Similarly we should expect the third term in Eqn. 4.7 to go to zero by $RM(\vec{a})$ and $RM(\vec{a} + \vec{\Lambda}_{SF})$ being uncorrelated. This tell us that for "seed points" at a fixed distance $|\vec{a}| = a$ the contribution of those points to the overall 2nd order structure function should be proportional to both $\sigma_{RM}^2(a)$ as well as the number of seed points at distance a.

Thus, in general we can calculate r_{eff} as

$$r_{eff} = \frac{\sum_i a_i N_i \sigma_{RM}^2(a_i)}{\sum_i N_i \sigma_{RM}^2(a_i)} \tag{4.8}$$

where i is over all sources being used in the structure function calculation, a is the projected distance to the RM source, N the total number of seed points within that source, and $\sigma_{RM}(a)$ can be obtained from the fitted profile to Eqn. 4.1. From our assumption that $\Lambda \propto n_e^{-\frac{1}{2}\eta}$ we can obtain Λ_0 by

$$\Lambda_0 = \frac{\Lambda_{SF}}{(1 + (\frac{r_{eff}}{r_c})^2)^{\frac{3}{4}\beta_c\eta}} \tag{4.9}$$

with r_c and β_c being obtained from the density profile, and η obtained from the fit to $\sigma_{RM}(a)$.

4.3 Estimating Magnetic Fields from σ_{RM}

We start by considering RM maps of the *g676* ICM calculated using using Eqn. 2.1 by integrating through the full simulation box. These would represent RM distributions for a background polarized screen. Figure 4.3 illustrates these distributions for three viewing angles corresponding to looking down the three principle axes of the grid. Large scale fluctuations are apparent in the core region of the cluster with individual values in excess of 1000 $rad\,m^{-2}$. RMs decline rapidly outside the core. The turbulent nature of the field is readily apparent in the maps by the patchy distribution of RM fluctuations.

To represent σ_{RM} as a function of radius, we calculate σ_{RM} over azimuthally averaged radial profiles from these background polarized screens. $\sigma_{RM}(a)$ is calculated over annuli of thickness 10kpc, with a representing the center of the annulus, and the annuli

evenly spaced logarithmically. The smallest radius is selected to be about half of a core radius. Observationally, a calculation over annuli in a cluster is not feasible due to the limited coverage of RM sources. However, for our simulated background screens, annuli should provide the best measurement of $\sigma_{RM}(a)$. Our choice of 10kpc thickness annuli is to ensure that sampling area is large enough to encompass multiple coherent RM patches (i.e. to ensure $|\langle RM \rangle| \ll \sigma_{RM}$), limiting statistical variations due to a lack of sampling multiple coherent patches. We calculate errors of magnitude $\frac{\sigma_{RM}(a)}{\sqrt{2N_{dof}-1}}$, where N_{dof} is set by the total sampling area divided by the sampling resolution. We arbitrarily pick $(4kpc)^2$ to represent the sampling resolution. The profiles for three different viewing angles are shown in Figure 4.4, one for each principle axis of the grid. For this idealized scenario, σ_{RM} profiles can differ by as much as a factor of 2 at cluster center, depending on the viewing angle and whether α is fit for or not. We will detail further the contributions to these errors in the following section.

We can also determine $\sigma_{RM}(a)$ by calculating σ_{RM} in boxes of a fixed size, and averaging the results based on box distance from cluster center. This calculation of $\sigma_{RM}(a)$ gives a better representation of an observational analysis, but can suffer from large statistical variation when $|\langle RM \rangle|$ approaches σ_{RM} within the boxes. If $|\langle RM \rangle| \ll \sigma_{RM}$ over all boxes, the $\sigma_{RM}(a)$ profile for this experiment should converge to the result obtained in the annuli experiment described above. Figure 4.4 shows the radial profile of σ_{RM} sampled over boxes of size 42x42 kpc^2. We place σ_{RM}, calculated within each box, into bins based on the box distance from cluster center. The boxes distance from cluster center is determined as the geometric mean distance calculated over all points located within the box. We then calculate $\sigma_{RM}(a)$ as the average σ_{RM} within the bin located at a distance a. The errors in $\sigma_{RM}(a)$ are 1-σ errors calculated over the σ_{RM} in each bin.

When comparing the $\sigma_{RM}(a)$ profiles for both annuli and boxes, we see that using 42x42 kpc^2 boxes produces similar results at small projected radii. However, further out from the core of the cluster, the two profiles diverge, with the box profile trending towards lesser $\sigma_{RM}(a)$. This is a consequence of the area sampled by the annuli and boxes being different at differing projected radii. For the annuli experiment, the sampling area increases proportional to a^2, while the sampling area of the boxes remains constant. It was argued in Section 2.3 that the RM coherence length should scale as $\Lambda \sim n_e^{1/2\eta}$. For

our cluster $\eta = 0.5$ and $\beta = 0.75$, that means outside the core, the RM coherence length should scale approximately as $a^{1/2}$. For annuli, as long as our innermost annuli has a large enough sampling area, $|\langle RM \rangle| \ll \sigma_{RM}$ for all sampled regions, which is seen in Figure 4.4. This will not be the case for boxes, where $|\langle RM \rangle| \gtrsim \sigma_{RM}$ when the linear size of the box becomes comparable to Λ.

To estimate $\sigma_{B,0}$, we fit profiles to both the annuli and box experiments using Eqn. 4.1. Two cases were considered, one treating both $\sigma_{RM,0}$ and α as free parameters, the other treating $\sigma_{RM,0}$ as fixed. In both cases, we used $r_c = 41.1kpc$ and $\beta_c = 0.75$ as obtained from the density distribution. In the α fixed case, we constrained $\eta = 0.5$, which is the known value from the 3D magnetic field distribution. The fitted profiles to the annuli data as well as $\frac{|\langle RM \rangle|}{\sigma_{RM}}$ for all three viewing angles and for free α are shown in the upper-left and lower left panels, respectively, of Figure 4.4. The fitted profiles as well as $\frac{|\langle RM \rangle|}{\sigma_{RM}}$ for both the box and annuli Z-axis viewing angle and for free α are shown in the upper-right panel of Figure 4.4. Numerical results are found in Table 4.1. In all cases, when α is treated as a free parameter, the average measured values of $\sigma_{B,0}$ are within $\approx 10\%$ of the actual 3D obtained value. However, there is a significant spread about the mean that in all cases spans about a factor of 2. The wide range is a result of the anisotropies present within the cluster. In particular, there is a large scale flow mostly aligned with the Y-axis of the grid that enhances both the density and parallel components of the magnetic field along that line of sight. When comparing the two models for Λ, we find that the density dependent model does a much better job overall of reproducing the η scaling value of the magnetic field with density. When we fix α, by the averaging it appears that the boxes do better at estimating $\sigma_{B,0}$. However, looking at each result individually shows that for the Z-axis and X-axis, the annuli experiment does very well (both cases within 10%) whereas the box experiment underestimates the field by as much as 50%. For the Y-axis case, both the box and annulus experiment overestimate $\sigma_{B,0}$ by over 50%. From these results, even with large sampling and well constrained parameters, ranges of up to a factor of 2 are obtained exclusively due to large scale anisotropies and inhomogeneities in the cluster. When $\frac{|\langle RM \rangle|}{\sigma_{RM}} \ll 1$ we expect the statistical uncertainties due to limited coverage of our regions to be small compared to cluster-scale anisotropies.

For embedded cluster sources, as it is very difficult to get line of sight positions to the

source within a cluster, it is often assumed that all embedded sources lie at the cluster mid-plane. As we are ultimately wanting to explore sources that lie within a cluster, we do the same experiment as above, but place the polarized screen at the cluster mid-plane. We consider 6 orientation of the polarized screen for each experiment, along the +/- x,y, and z axes. The results are provided in Table 4.1. The results for α as a free parameter for both the mid-plane and annuli experiment are further shown in Figure 4.5. The results are largely consistent with the background screen experiments with the exception of larger ranges in the estimated $\sigma_{B,0}$. However, the results for $\sigma_{B,0}$ are on average lower when compared to the background scenario. This is because the + / - pairs of screens are correlated due to their sampling similar regions at cluster center. This is reflected in our assumption that the mid-plane screen $\sigma_{B,0}$ estimates should be $\sqrt{2}$ times smaller than the background, as this assumes no correlation between the front and back half of the cluster.

To mimic actual observational data, we create a third scenario where multiple, non-interacting RM sources are embedded within our cluster volume. For actual observed radio sources, there is usually no information of the positions along the line of sight. So, we perform the analysis assuming all sources are located at the cluster mid-plane. As with the mid-plane scenario, we use projected viewing angles looking along the plus and minus x, y, and z axes of the grid. This allows us to compare estimated magnetic fields using randomly sampled RMs to the previous analyses that have RMs filling the cluster. To account for statistical uncertainties based on total sampling area, we conduct three embedded source experiments: one containing 3 embedded sources, another 8 embedded sources, and the third 14 embedded sources. An example of an RM map obtained from 8 embedded sources is shown in Figure 4.6. The sources are placed so that their average line of sight position places them roughly at the cluster mid-plane. The overall size of the sources vary, the typical linear size across a source is $\sim$20 kpc and ranges from 5kpc to 50kpc and is chosen to be representative of the size of a typical non-central radio source. We calculate Λ through Eqn. 4.6 where $\Delta\vec{a}$ are allowed both within a source and across sources. Thus, we produce one structure function and one Λ_{SF} for each viewing angle, where the viewing angles again consist of the + and - X, Y, and Z axes. From this we obtain an Λ_0 through Eqn. 4.9. When fitting $\sigma_{RM,0}$, we include errors at each data point that include a $\sim \frac{1}{\sqrt{N_{dof}}}$ component as above, as well as a constant $5 rad m^{-2}$

component to reflect the limitations you would expect on observational measurements of σ_{RM}. These two error components are added in quadrature to get the total error. We display the resultant $\sigma_{RM,0}$ from the fits in Table 4.2. Reported ranges of the fitted $\sigma_{RM,0}$ will have the lowest and highest values of $\sigma_{RM,0}$ removed. As we have 6 data points (one for each viewing angle) for each set of sources, we can treat the two most extreme values as outliers, and the inner 4 data points as an approximation to 1-standard deviation from the mean.

Fits to the RM map in Figure 4.6 are shown in Figure 4.7 considering both α as a free parameter and fixed α corresponding to $r_c = 41.1 kpc$, $\beta_c = 0.75$. We find that the limited sampling offered even with 14 sources does not allow for a proper treatment of η as a free parameter as unphysical values, both low and high, of η (and as a consequence $\sigma_{RM,0}$) are produced. The resultant $\sigma_{RM,0}$ and as a consequence $\sigma_{B,0}$ span over an order of magnitude. In some cases, a value of η obtained is negative, which corresponds to an unphysical result. Thus it seems necessary that for a random sample of RM sources in a cluster that a physically motivated α value, or range of values, must be selected to get reliable estimates of the central magnetic field dispersion.

Observationally, small sampled regions producing $|\langle RM \rangle| \gtrsim \sigma_{RM}$ give poor statistical results when trying to measure global magnetic fields from a fitted RM profile. Often, the observational data is compared to RMs produced from modeled magnetic field and density distributions Murgia *et al.* (2004). These modeled RMs are calculated over boxes of similar size to the observed RM sources and the RM profile from these boxes is fit to the observed RM data. To emulate this, we can compare the profile resulting from boxes of similar size to the sources to the profile fit to the embedded RM data. Using the simulation as our model, we can verify that comparing our embedded sources RM profile to that of the boxes produces agreement in the resulting $\sigma_{RM,0}$ values. The average linear size across an embedded source is ~ 20kpc, so we would expect that boxes of size $20 \times 20 kpc^2$ should produce $\sigma_{RM,0}$ most consistent with the embedded source experiment. Table 4.2 lists the average and range of $\sigma_{RM,0}$ values obtained for all three embedded source experiments as well as the results from differing box sizes. As our expectation, the average and range of $\sigma_{RM,0}$ are most closely approximated by the 24kpc boxes. We also observe that the results of both the 8 source and 14 source experiments show almost identical results, suggesting sampling convergence. Given the

similar uncertainty range when compared to boxes or annuli, this suggests that as long as the average line of sight distances of the sources is that of the cluster mid-plane, no bias or uncertainty should be expected from line of sight uncertainties when calculating $\sigma_{B,0}$.

Considering the above, the estimated cluster $\sigma_{B,0}$ and η obtained by power law modeling of the magnetic field are likely to produce similar results as when using models of more complicated field spectrum represented by a characteristic scale. In fact, the power law modeling can also be similarly represented by a single scale as defined by Λ_{CR} above. As long as Λ_{CR} is consistent between the two models, the estimates should largely agree. However, the only parameters of the magnetic field necessary to create an effective model are Λ_{CR}, $\sigma_{B,0}$, and η. Because the power law model may not be an accurate representation of the cluster magnetic field spectrum, caution is suggested when applying further parameters of a power law magnetic field model (such as inner and outer scales, and the power law index) to the physical properties of the cluster. It is suggested that the Λ of Eqn. 2.2 be viewed as a parameter that satisfies the equation and not be directly attributed to any physical property within a cluster.

Furthermore, the variable coherence length model suggested should be considered in further modeling. Recently, Bonafede *et al.* (2013) showed that current magnetic field models underestimate the RM strengths at large projected radii in the Coma cluster. Given the estimated values of β_c and η for Coma, roughly a factor of 2 increase RM profiles could be obtained from a variable Λ model at these large radii. While this doesn't account for the entire factor of 3-4, it may suggest the amount of field amplification needed might not be as strong as suggested.

4.4   Uncertainty Contributions to $\sigma_{B,0}$

We highlight uncertainty contributions in the estimates of the cluster magnetic field. For our randomly embedded source experiment, there are five separate contributions to the uncertainty: uncertainties associated with the least-squares fits, uncertainties from large scale anisotropies in the gas and magnetic field distributions in the cluster, uncertainties from the constraint to the η parameter, uncertainties due to the inability to constrain the line of sight positions of the source, and uncertainties in determining Λ in

the cluster. Our goal is to emphasize which uncertainties are unavoidable in estimating magnetic fields through an RM analysis. Of these uncertainties, those associated with the least-squares fit are $\lesssim 1\%$ for all of our experiments and can be ignored.

We first explore the errors associated with the RM coherence length, Λ. By Eqns. 2.2, & 4.3, the magnetic field estimates should scale as $\sqrt{\Lambda}$. For our filled mid-plane screen experiments, the range of obtained Λ_{SF} and as a consequence Λ_0 spans a factor of $\sim 25\%$. Our random embedded source experiments have more limited sampling, and the range of obtained Λ_{SF} & Λ_0 spans a factor of ~ 3. Thus, in the filled mid-plane screen experiments, the associated errors about the mean estimated field due to uncertainties in Λ figure to be $\sim 12\%$. For our randomly embedded experiments, this increases to $\sim 35\%$-40%. Thus, in a best case scenario, for embedded (and likely background) RM experiments in clusters, a reasonable best case scenario suggests 35% errors solely due to uncertainties in Λ.

Errors associated with cluster scale anisotropies have been suggested in Section 2.2. We can most readily see the magnitude of these errors from the results of the mid-plane screens fixing $\eta = 0.5$. These experiments are presumably only impacted by fit errors (which we have already claimed are small), anisotropic errors, and errors in Λ. We see from the results that the range of estimated σ_B spans about a total factor of 2. Thus, there is a total error about the mean of $\sim 50\%$. We know that of this total error, about 12% is due to uncertainties in Λ. That means errors associated with anisotropies in the cluster are about 45%.

The errors associated with the uncertainties in the line of sight positions of the sources can be explored by noting the range of $\sigma_{RM,0}$ (Table 4.2) values obtained in the random embedded source experiments. As the $\sigma_{RM,0}$ values can be fitted directly from the sources, the contributing errors are from line of sight errors, fit errors (negligible), anisotropic errors, and errors in η. However, in our random source experiments, we suggested restricting α, and we have done so to the known cluster value and introduce no errors associated with η as a result. When this is done, the spreads in the σ_{RM} data are comparable to that when RMs fully sample the cluster. So, our errors are still dominated by cluster scale anisotropies.

When calculating $\sigma_{B,0}$, by Eqn. 4.3, we see that the results are most strongly dependent on $\sigma_{RM,0}$, and only very weakly dependent on α. Thus, even if α is well

constrained, you are limited by how well you can estimate $\sigma_{RM,0}$. However, $\sigma_{RM,0}$ is very sensitive to the cluster scale anisotropies that in our cluster contribute the most significant error. So, even with ideal observational data, it is suggested that the best case scenario is 50% errors in $\sigma_{B,0}$ estimates solely by being limited to one viewing angle of the cluster.
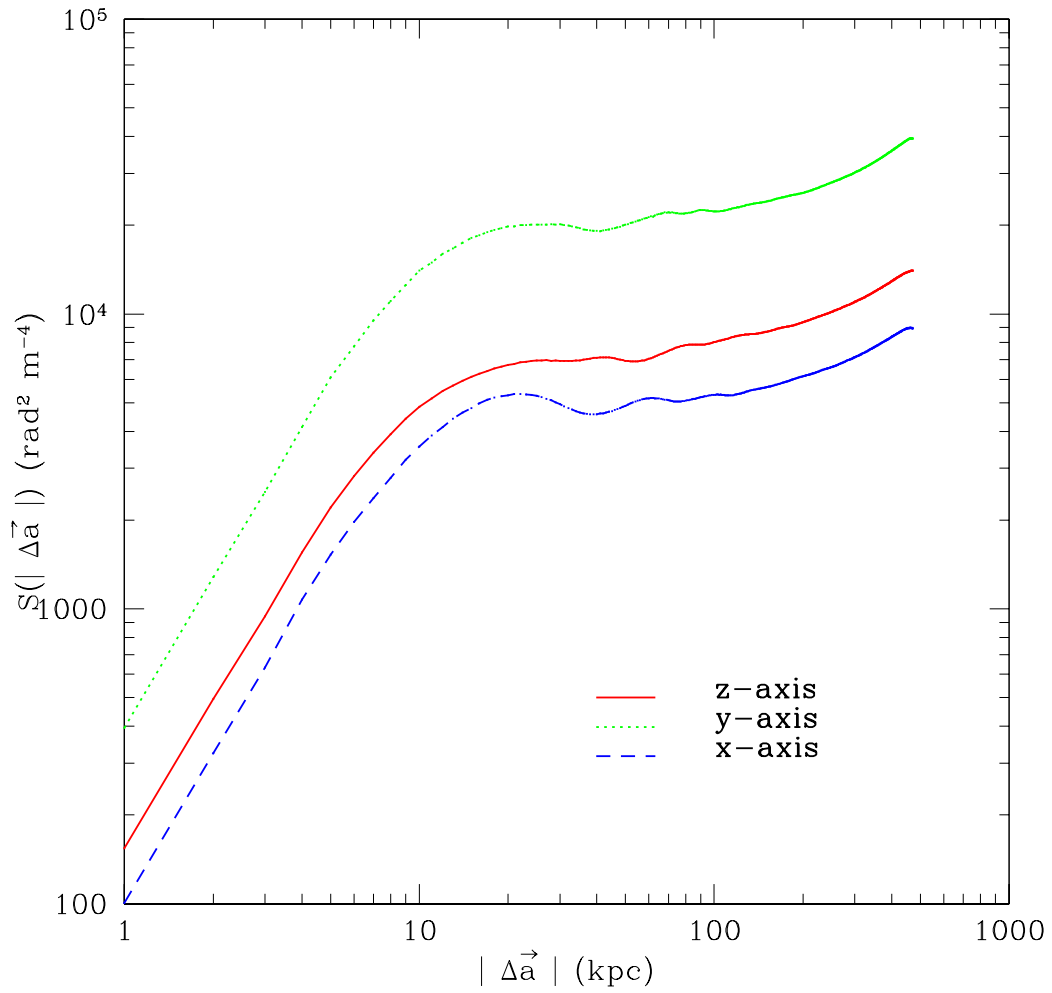
4.5   Figures

Figure 4.1 2nd order structure functions of the RM distributions calculted over the entire simulation. The axis displayed for each line corresponds to the viewing angle of the grid for the RM distribution.
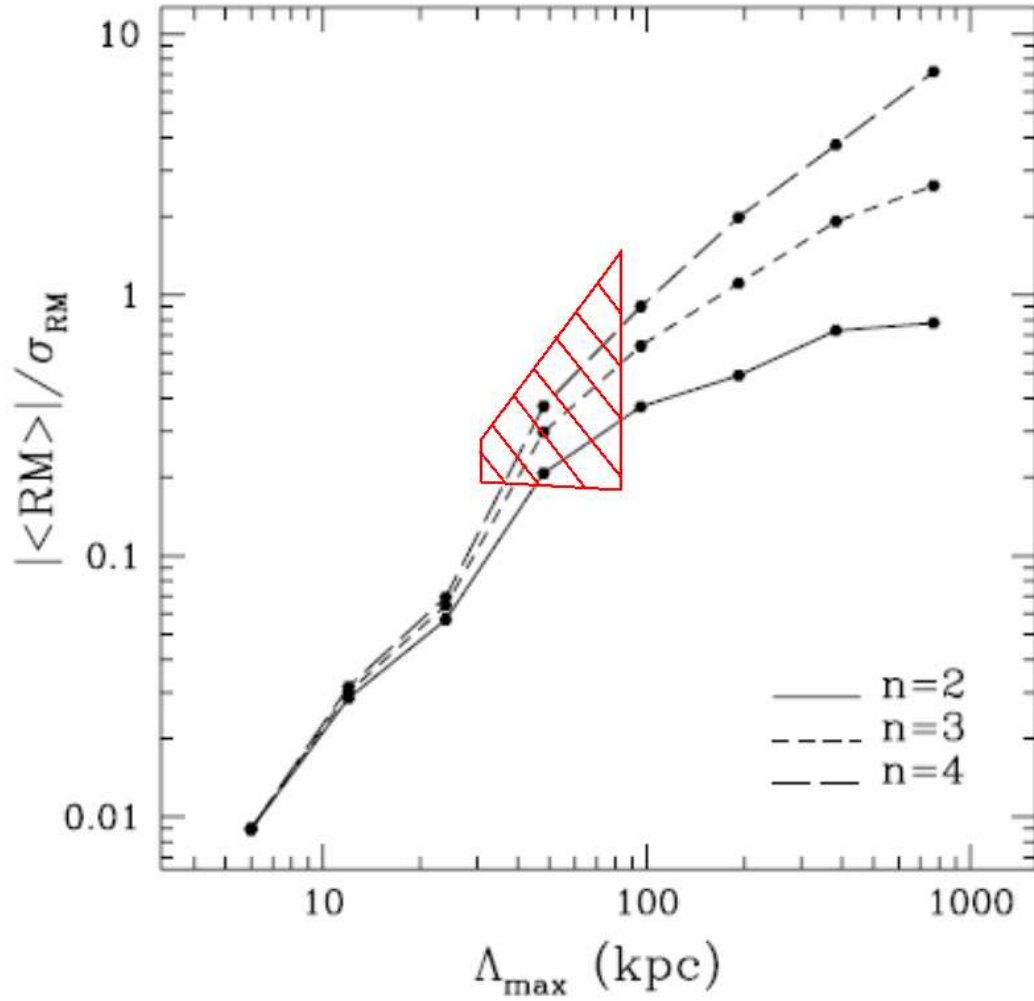
Figure 4.2 $\frac{|\langle RM \rangle|}{\sigma_{RM}}$ compared to the magnetic coherence length, Λ (Λ_{max} in figure). The base figure was obtained from Murgia *et al.* (2004) who used 50kpc x 50kpc boxes sampled from a cluster with a power law RM power spectrum of index n. The results from our simulation used 42kpc x 42kpc spanning 6 different viewing angles of the cluster and are shown in the shaded region, which depicts the 90% confidence level for a given box.
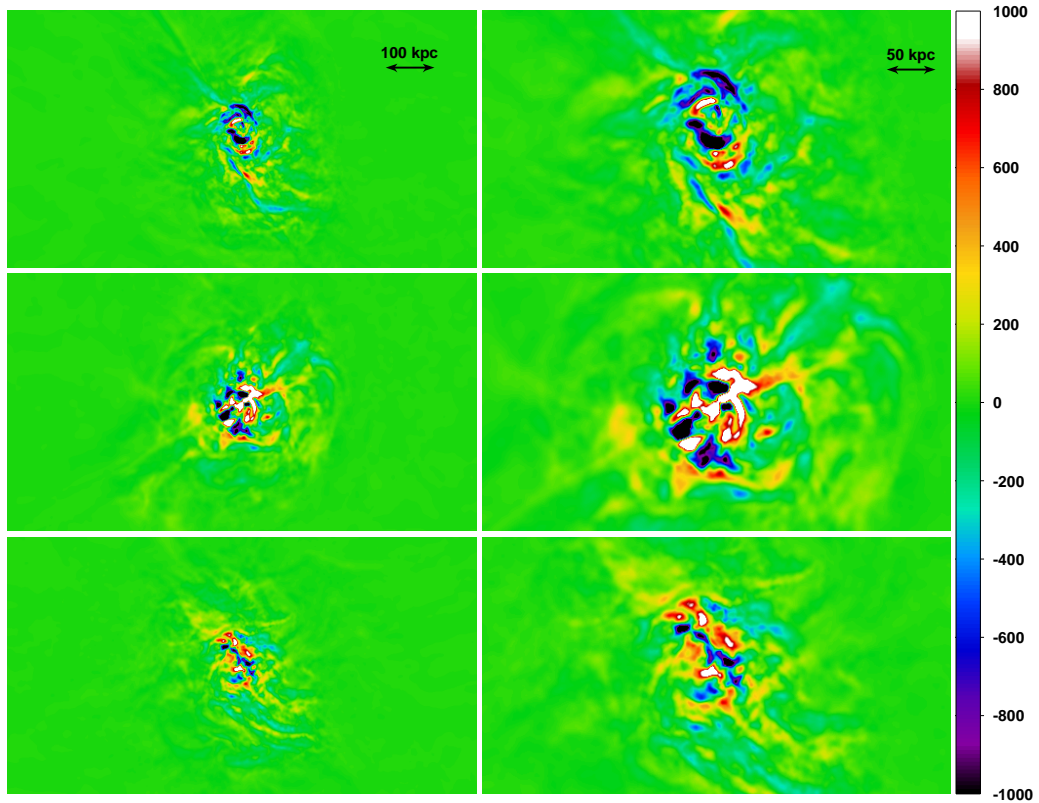
Figure 4.3 Map of the cluster RMs obtained by integrating through the whole grid along the z-axis (top), y-axis (middle), and x-axis (bottom). The left column shows the entire simulation box spanning 1 Mpc horizontally. The right column zooms in on a volume covering the inner 200 kpc (horizontally) of the cluster to highlight the strong RM fluctuations in the core region of the cluster. The colorbar scale is in units of radm^{-2}.
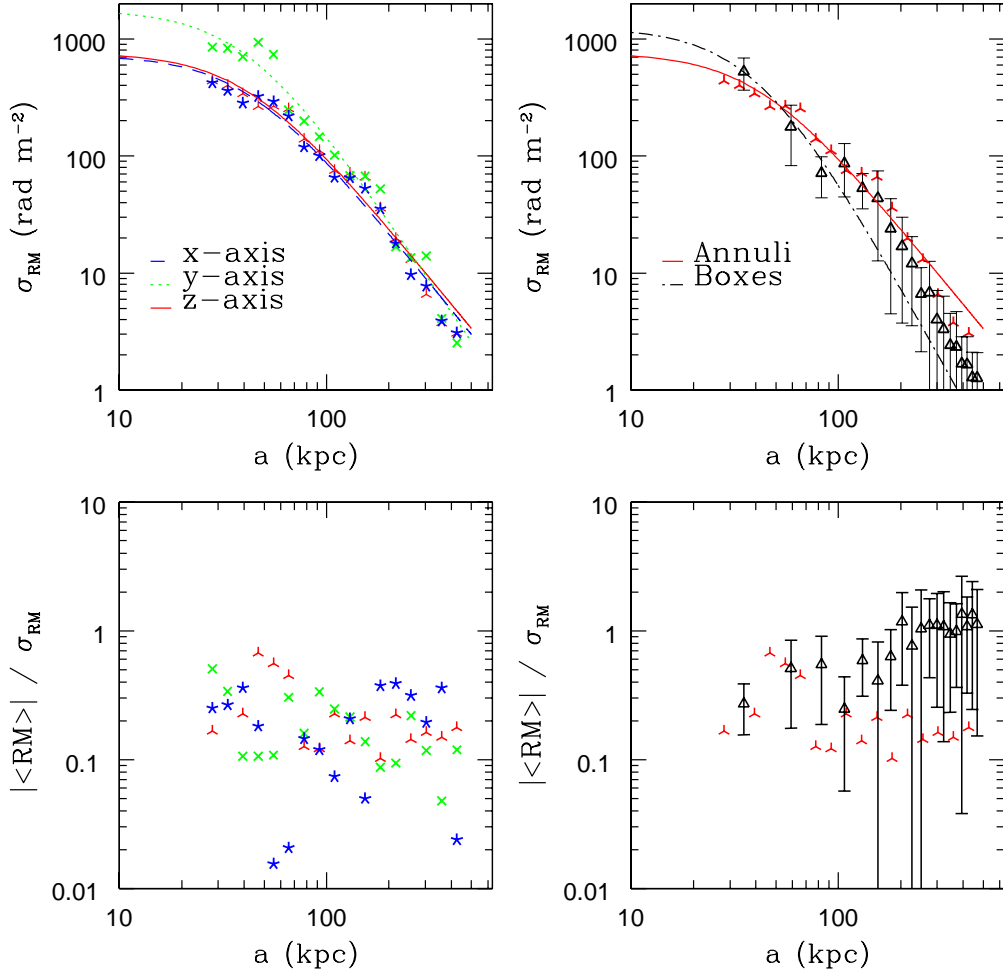
Figure 4.4 Fits to the background screen σ_{RM} are shown in the top left panel for projected angles down the Z-axis (triangles), Y-axis (x's), and X-axis (stars). The data points are separated logarithmically and are calculated over annuli of thickness 8 kpc. The upper right panel shows the σ_{RM} distribution calculated over both annuli as well as for 42kpc x 42kpc boxes, both looking down the Z-axis. The lower left panel displays $|\langle RM \rangle|/\sigma_{RM}$ for the background screen using annuli. The lower right panel displays $|\langle RM \rangle|/\sigma_{RM}$ for the background annuli experiment (starred data points) as well as for a boxes experiment (closed data points) using the same viewing angle. Errors for the annuli data points in all frames are of the symbol size or smaller.
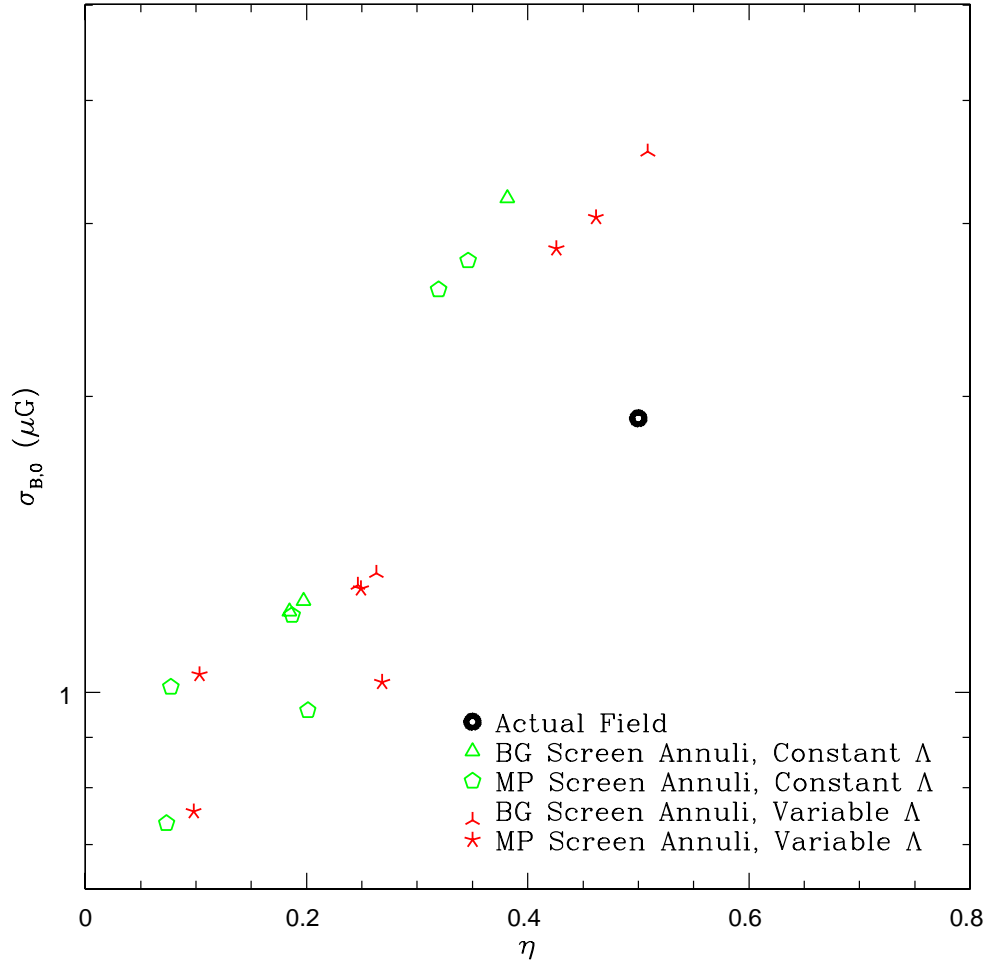
Figure 4.5 Estimated values of $\sigma_{B,0}$ and η by calculating σ_{RM} in annuli from both the mid-plane (5-point) and background (3-point) screen experiments. The comparison is to be made between using a constant Λ model and density dependent Λ model. The black circular data point shows the actual value of the 3D magnetic field.

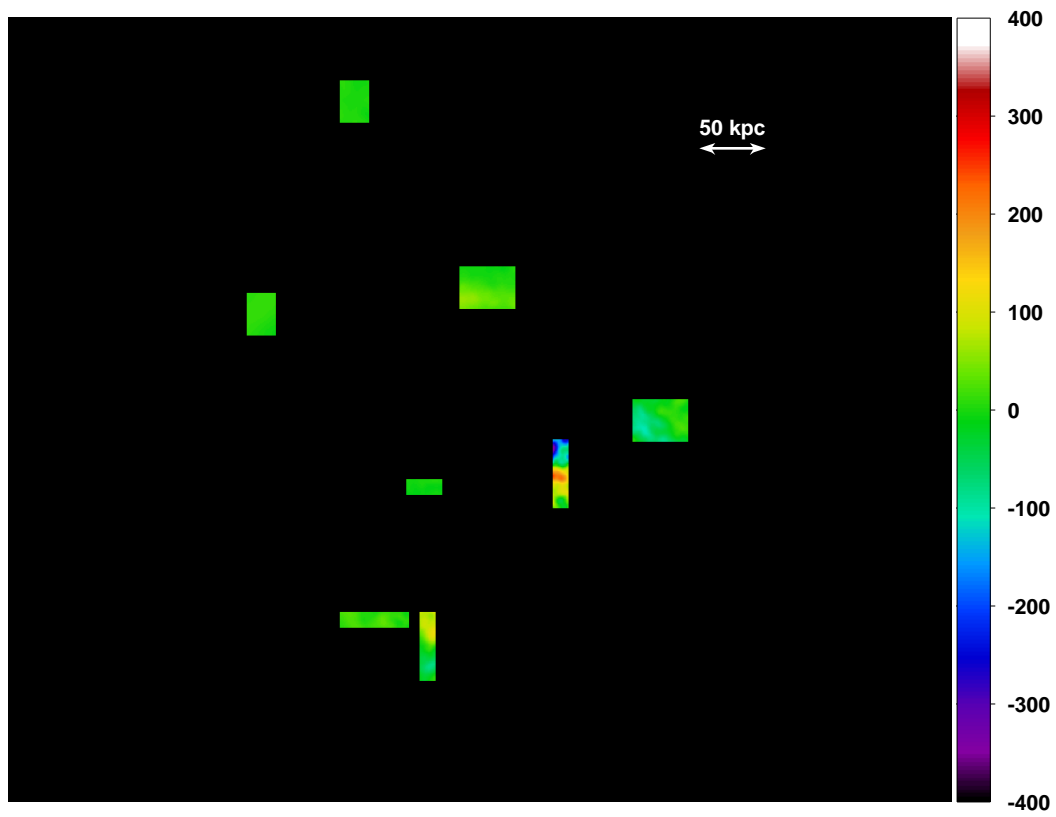Figure 4.6 A map of the RMs from 8 randomly distributed sources looking down the z-axis of the grid. The colorbar scale is in units of $\mathrm{rad\,m^{-2}}$.
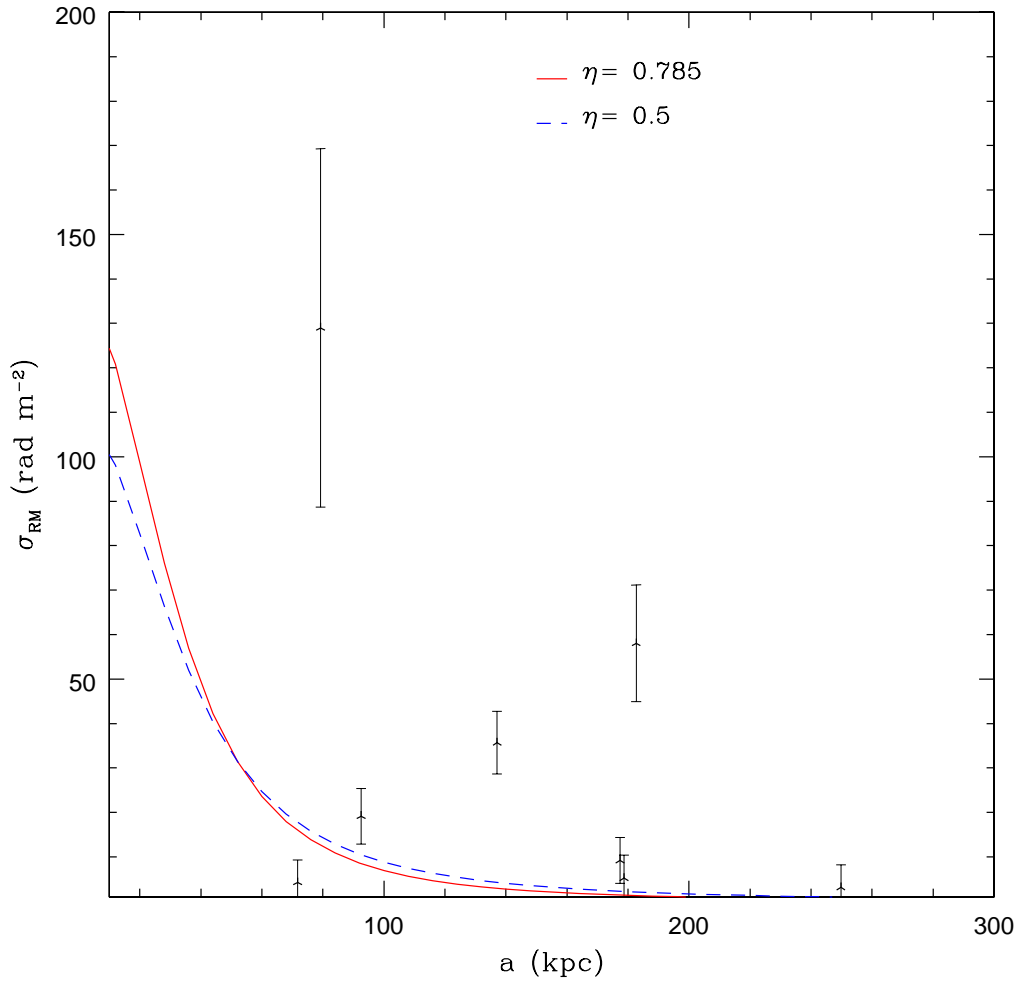
Figure 4.7 Fits to the RM data are shown for a scenario of 8 randomly embedded sources along the Z-axis with the solid line corresponding to treating η as a free parameter and the dashed fixing $\eta = 0.5$.

Table 4.1.   Filled Screen $\sigma_{B,0}$ Statistics.

	$\langle \Lambda_0 \rangle$	$\langle \sigma_{B_{0,0.5}} \rangle$	$range(\sigma_{B_{0,0.5}})$	$\langle \sigma_{B_0} \rangle$	$range(\sigma_{B_0})$	$\langle \eta \rangle$	$range(\eta)$
Constant Λ							
BG Annuli	22	2.97	2.40-4.10	1.87	1.24-3.18	0.25	0.18-0.38
MP Annuli	23	2.67	1.79-3.72	1.54	0.96-2.57	0.20	0.07-0.32
BG Boxes	22	1.87	1.27-2.84	1.76	0.92-2.63	0.46	0.30-0.65
MP Boxes	23	1.35	1.13-1.70	1.21	0.70-2.06	0.38	0.32-0.46
Density Dependent Λ							
BG Annuli	17	2.55	2.04-3.50	2.05	1.29-3.55	0.34	0.25-0.51
MP Annuli	18	2.32	1.58-3.21	1.66	1.02-2.83	0.27	0.10-0.43
BG Boxes	16	1.83	1.21-2.81	2.09	1.06-3.11	0.62	0.41-0.86
MP Boxes	16	1.37	1.10-1.64	1.43	0.82-2.44	0.50	0.43-0.61

Note. — Statistical values of the estimated magnetic field properties determined from both polarized background (BG) or mid-plane (MP) screens in the cluster at the initial conditions. Averages and errors are calculated over all projected angles for a given experiment. The values of σ_B are in μG and RM coherence length scales are in kpc. The second subscript in $\sigma_{B_{0,0.5}}$ corresponds to the assumed fixed $\eta = 0.5$. The value of σ_{B_0} without the second subscript corresponds to the fitted value assuming η a free parameter. The range incorporates all 3 projected angles for the BG case and only 4 of the 6 projected angles for the MP case with the 2 extreme data points excluded. The fit to the actual magnetic field in the cluster yields $\sigma_{B_0} = 1.9 \mu G$ and $\eta = 0.5$.

Table 4.2.   Random Passive Source $\sigma_{RM,0}$ Statistics.

	$\langle \Lambda_0 \rangle$	$\langle \sigma_{RM,0} \rangle$	$range(\sigma_{RM,0})$
Embedded Sources			
3 Sources	16	526	375-627
8 Sources	21	462	344-538
14 Sources	21	462	341-550
Mid-plane Screen Boxes			
12kpc	16	386	269-489
24kpc	16	521	354-720
42kpc	16	601	460-718
56kpc	16	665	442-705
84kpc	16	836	563-878

Note. — Statistical values of the estimated $\sigma_{RM,0}$ for 3, 8, or 15, randomly embedded passive sources as well as for boxes of various linear sizes. Averages are calculated over all projected angles for a given experiment. Ranges incorporate only 4 of the 6 projected angles for each scenario, with the 2 extreme data points excluded. The values of $\sigma_{RM,0}$ are in $rad\,m^{-2}$ and Λ_0 in kpc.

Chapter 5

Interacting Radio Source Analysis

In this section, we investigate the influence of a cluster centered AGN on the local ICM magnetic fields and density and how this impacts the observed RMs. To achieve this, we run simulations of a dynamic cluster with a central AGN that interacts with the surrounding ICM. We will explore how both the epoch of jet launching as well as the amount of introduced magnetic fields from the jet influence RM measurements made from the resulting radio emitting regions. Using the analysis outlined in Chapter 4, we then try and estimate the ICM field properties with the interacting source.

5.1   Numerical Setup

We use the cluster *g676* as described in Chapter 3 and used in the analysis of Chapter 4 as our initial conditions. Each simulation spans 200 Myr and evolves the cluster using the WOMBAT MHD code (Mendygral *et al.*, 2012). The simulations are placed on a 1008^3 grid centered on the cluster dark matter peak, which we define as the cluster center. The grid has a uniform resolution with $\Delta x = \Delta y = \Delta z = 1$ kpc. Boundary conditions were based on those used in O'Neill & Jones (2010). The initial ICM was created without radiative cooling; similarly, our simulations assumed an adiabatic equation of state with $\gamma = 5/3$. We confirmed that radiative cooling effects would not have been significant over the span of our WOMBAT simulations. Two of the simulations have a placed AGN at the cluster center which launches intermittent, bipolar jets into the ICM. Those simulations, which we label, *Beta100* and *Beta001*, will be described below.

They differed only in the strength of the magnetic field carried by the jets. In order to measure the influences of the AGN outflows we carried out a comparison simulation that was identical to the other two except that the AGN was not present. In other words we evolved the initial state of the ICM in the presence of the assumed gravity, but no applied disturbance. We identify that as the *NoAGN* simulation.

The *Beta100* simulation was, in fact, the **R1** simulation discussed in Mendygral *et al.* (2012). Readers are referred to that paper for full details. Here we provide only a brief outline necessary to understand the results of the present work. Again, the *Beta100* and *Beta001* simulations are identical in every respect except for the strength of the jet magnetic field. The jets are launched with a 50% duty cycle in a 26.2 Myr period from a cylinder of radius, $r_j = 3$ kpc. and length $l_j = 8$ kpc on each side of the AGN position. Although the orientation of the cylinder was arbitrary, it turned out to be almost perpendicular to the bulk flow of ICM, which led to substantial deflections of the jets as they propagated (cf., Mendygral *et al.* (2012)). After six cycles, so about 157 Myr, jet launching ceased; there was no additional AGN activity during the final 43 Myr of these two simulations. The jet density in the active launch cylinder was set to $\rho_j \approx 4 \times 10^{-28}$ g cm^{-3}, and the gas pressure was approximately the local ICM pressure. At peak power the jet velocity was 0.03c, corresponding to an internal jet Mach number, $M_j = 1.2$ and a power per jet, $L_j \approx 3 \times 10^{44}$ erg s^{-1}. The total energy injected onto the grid by the jets was approximately 2×10^{60} erg. We did not attempt to determine details of energy transfer between these jets and the ICM. However, our previous, similar simulation studies (O'Neill & Jones, 2010) indicated that roughly $10 - 20\%$ of the power of intermittent jets was immediately transferred to ICM kinetic energy, while about double that fraction went directly into heating the ICM. We expect similar rates apply here, so provide crude measures of the energy these jets added to the cluster ICM. For comparison, the thermal energy content of the *g676* cluster was $\approx 6 \times 10^{61}$ erg. Thus, it is clear that these jets had the capability to modify the ICM, including its density and magnetic field structures significantly.

The magnetic field injected by the jet launch cylinder was toroidal, with the same polarity in both jets. The field vanished on the jet axis as well as on the outer boundary of the launched jet. The peak magnetic field in the *Beta100* simulation was $B_j \approx 8$ μG, corresponding to a plasma $\beta = 8\pi P_j/B_j^2 = 100$. The peak magnetic field in the *Beta001*

simulation was 10 times stronger, so that $\beta = 8\pi P_j / B_j^2 = 1$. We outline three different epochs in the jet launching below: at 80 Myrs (AGN currently in an off cycle), 92 Myrs (AGN currently starting on cycle), and 200 Myrs (AGN inactive for 43 Myrs). RM maps for each run at each epoch are made using 8 different projected angles, 6 along the principle axes of the grid, in which the jet has an inclination angle of 45^0, and two arbitrary angles that have an inclination angle of 0^0. An inclination angle of 0^0 corresponds to the jet axis being in the plane of the sky.

5.2 Physical Modifications

The AGN activity produces a significant amount of entrainment within the radio lobes. Figure 5.1 shows a slice through the radio lobes displaying the fractional mass mixing of jet plasma with ICM plasma. The multiple "banded" structures present are due to the intermittent launching of the jet. As the evacuated cavities (which would be seen as X-ray cavities observationally) expand out into the cluster, the jet plasma hits the forward contact discontinuity and then wraps around the edge of the cavities back towards the cluster center. This produces a "mushroom cap" (see Mendygral *et al.* (2012)) structure at the head of either side of the radio source. With each cycling of the AGN, ICM material gets pulled in from behind the jet. This material forms a boundary layer between the current jet cycle and subsequent jet cycles.

During the on-phase of the jet cycle, a boundary layer with numerical thickness $\sim$4 zones thick forms between the collimated outflow and the entrained ICM. This boundary layer remains stable along the jet column while the jet is active. Where the jet column meets the forward contact discontinuity, the jet gets disrupted and physical mixing, analogous to that seen in Kelvin-Helmholtz simulations, occurs between the jet plasma and the entrained ICM. Outside of the jet column, it is rare for the mixed plasma to be more than 50% jet plasma by mass indicating the mixing of ICM within the jet lobes is significant. The highest concentrations of jet plasma are located in the collimated jet while the AGN is active, or in a region that piles up at the direct head of the forward contact discontinuity, indicating the jet plasma is largely unmixed until the jet gets disrupted.

We also explore how the jet influences the density structures in the cluster. Figure

5.1 shows the difference between the density in the presence of a central AGN (*Beta100*, *Beta001*) and the density of a naturally evolved cluster (*NoAGN*) in a slice through the jet region. The large scale patterns seen in these slices are largely independent of the β parameter of the outflow. We are able to see a clear boundary between areas of reduced density (marking the evacuated cavity) and regions where there has been compression. The region outside the cavity contains ICM that has been displaced from the evacuated cavity and experiences compression. This region lies behind a forward bow shock that is created from the launching of the jet. As expected, most of the compression occurs immediately behind the head of the bow shock. Beyond the bow shock, the ICM is completely uninfluenced by the presence of an AGN. All of the jet plasma, and hence, source of polarized emission is located within the evacuated cavity and is unable to traverse the leading contact discontinuity.

The magnetic field structure introduced by the jet is necessarily dependent on the jet plasma β. We look at the three components of the field in a cylindrical coordinate system $B_{\bar{s}}$, $B_{\bar{\phi}}$, and $B_{\bar{z}}$, where $\bar{z}$ is along the jet axis. To analyze the field, we construct concentric cylindrical shells, who's center axis aligns with $\bar{z}$, of thickness $4kpc$, length of $300kpc$, and radius s and calculate statistics on each component of the magnetic field within the shells. We then compare each component of the field when the AGN is present (either *Beta001* or *Beta100*) to the components of the naturally evolved cluster (*NoAGN*). This allows us to see how each component changes due to the presence of an AGN as we get further away from the jet axis.

Figure 5.2 shows this behavior for each β and at the 92 Myr epoch. Where the lines converge corresponds to the region of uninfluenced ICM which lies both outside the evacuated cavity and beyond a region where local ICM gets compressed behind the bow shock. For the *Beta100* jet, the magnetic fields shows no significant amplification other than very near the jet axis for the z-component. This is purely from ambient magnetic field being dredged along with the ordered flow from the jet column. Otherwise, very little field amplification or redistribution occurs. For *Beta001*, we see significant increases of the magnetic fields within the cavity region. This is predominantly due to the introduction of strong magnetic fields from the jet itself. This is accentuated by the very strong toroidal (ϕ) component increase. The introduced jet material has a toroidal field associated with it, so it is expected that the toroidal component should see the

largest change within the cavity. As our distances get farther away from the cavity, we start probing areas outside the cavity, and as in the *Beta100* case, little modification is observed. The behavior is similar at other epochs of jet launching.

5.3   Observational Modifications

We compare RMs from both *Beta100* and *Beta001* with those from *NoAGN*. The RM maps from *Beta100* and *Beta001* are calculated along each line of sight using two different masks. The first mask considers a "full path screen" which integrates from the back side of the jet cavity towards the observer. The second mask considers a "foreground screen" which integrates from the near edge of the cavity towards the observer. To define the back edge of the cavity, we determine the farthest point from the observer where the fraction of jet plasma to ICM plasma (color) is greater than 1%. To define the near edge of the cavity, we determine the nearest point where the color variable becomes greater than 1%. For each of these masks for both *Beta100* and *Beta001*, a corresponding RM map from *NoAGN* is created with the same integration path lengths. The purpose of the foreground screen mask is to show how the RMs would behave if the jets probed *only* only regions of ICM in front of the jet lobes.

Figure 5.3 shows the RM maps for a foreground *Beta100* and corresponding *NoAGN* map as well as a full path *Beta001* and corresponding *NoAGN* map. The RM patterns between the foreground screen *NoAGN* and *Beta100* show strong similarities. As we have shown above, there is little modification of the magnetic field outside of the jet cavities. Thus, the only significant contribution of the jet outside the cavity is to compress the ICM behind the forward shock. For the full path *Beta001* we get strong contributions from the evacuated region, and a clear asymmetry is seen about the jet axis in the RM distributions. Very little of the RM structures seen in the *NoAGN* comparison are seen in the *Beta001* RM map. This asymmetry is to be expected from the strong introduced magnetic fields from the jet and the preservation of field polarity described in the previous section. The strong contribution from the evacuated cavity is a result of the strong magnetic fields tied to the jet plasma being able to offset the low density of the jet plasma/ICM mixture.

An example of the RM profiles are displayed in (Figure 5.4) at $t = 80 Myrs$ and $t =$

$92 Myrs$. In all cases, the foreground screens for all three simulations are comparable. This means that if there is no contribution from the jet cavities, the presence of a jet does little to modify the RM structures present within the cluster. For *Beta100*, the full path mask is very similar to the foreground mask, which suggests that the cavity region contributes very little to the overall RMs. This is due to the cavity being largely evacuated while maintaining roughly the same magnetic field structures as if no AGN had been present. In contrast, *Beta001* shows increased RMs for the full path case over *NoAGN*. This is because, while the cavity is still evacuated, strong magnetic fields from the jet have filled the cavities, and the net effect is a strong RM contribution from within the jet cavities.

5.4   Measuring the Cluster Field

We follow the same approach to measuring the cluster field as outlined in Chapter 4. We will assume that observationally we would not have any information about jet orientation within the cluster. Thus, in determining the path length, we can make the usual assumption that the jet axis lies in the cluster mid-plane. As with the random source analysis in Chapter 4, we obtain the central RM coherence length, Λ_0 from Eqn. 4.9 by calculating an r_{eff}. β-profiles are fit to the cluster density profile of *NoAGN* at the appropriate epoch of the jet, and for each epoch, we will obtain a unique n_0, r_c, and β_c. Magnetic field estimates including η as a free parameter suffers from the same issues as seen in the random sources, often producing unphysical results. Thus we will focus on keeping η, and as a result α, fixed to one of two values, using $\eta = 0.5$, or the real η value of the 3D field at the time considered.

The results for the magnetic field estimates are summarized in Table 5.1. We only include the *NoAGN* mask compared to the *Beta100*. As the boundaries of the color variable are largely similar between *Beta100* and *Beta001* the masks for either foreground or full path are almost identical between the two *NoAGN* masks. Due to the size of the jet lobes, we are able to sample many regions of sufficient size to ensure $|\langle RM \rangle| \ll \sigma_{RM}$. Thus our $\sigma_{RM}(a)$ profile is expected to converge to the mid-plane annuli profile described in Chapter 4.3. We see that all foreground results produce values that are on average lower than real value. These underestimates give central

magnetic field dispersions that average up to 40% lower than the real magnetic field for the cluster. This can be reconciled by noting that the cavity has width to it and does not contribute to RMs for the foreground screen and *Beta100*. Assuming a cavity that is symmetric about ϕ in cylindrical coordinates, we can define r_{cavity} as half the projected distance across the jet cavity perpendicular to the jet axis. RM contributions occur only in front of the cavity, which occurs at a distance $\frac{r_{cavity}}{sin(i)}$ in front of the jet axis, where i is the inclination angle of the jet to our line of sight. Thus, in our case, the r_{cavity} is on order of r_c, and since on average, our integration starts a core radius in front of the mid-plane, these low value should not be unexpected.

For the full path *Beta001*, the estimated field ends up being greater than the known values on average by $\gtrsim 30\%$ and by as much as a factor of two.. The result of this is from the significant RM contribution within the jet lobes due to the strong fields tied to the jet plasma and in conjunction with the jet plasm/ICM mixture. Given the physics and set up of our cluster, it is hard to justify an accurate estimate of undisturbed ICM fields when the fields contribution from the jet plasma is strong, as the contributing RMs are going to be largely dependent on the parameters of the jet plasma such as the plasma β and the jet-ICM mass ratio. Candidate sources that seem to contain significant radio source-ICM interaction are discussed in Guidetti *et al.* (2011, 2012).

Our analysis can be related to the work performed in Huarte-Espinosa *et al.* (2011) through our fixed η models. In their analysis, they also produced a jet that modified a local turbulent ICM. Their RMs considered contribution from the ICM in front of the evacuated cavity similar to our foreground screen masks. In particular, our *Beta001*, and *Beta100* models are most similar with their low jet density, low Mach number models. Their models have a β value in the jet plasma that is on average of about 10, which is between our values of 1 and 100. A β of 10 still describes a kinetically dominated jet, which would best be approximated by our *Beta100* model. If we look at our *Beta100* models, which have little contribution from the radio lobes, we find $\frac{\langle \sigma_{RM,jet} \rangle}{\langle \sigma_{RM,mask} \rangle} \sim 1.2$, where averages are are over all lines of sight, and we fix $\eta = 0.5$. This agrees with their assertion that the amplification of RMs is most significantly a result of compressed ICM beyond the evacuated cavities. Looking at $\frac{\langle \sigma_{RM,jet} \rangle}{\langle \sigma_{RM,mask} \rangle}$ for *Beta001*, we find that values are ~ 1.9 when compared to the jet-axis mask, and ~ 2.5 when compared with the foreground mask. These values are higher than those reported in Huarte-Espinosa *et*

al. (2011). The higher values come from significant RM values being produced within the radio source itself as well as stronger compression for smaller values of β in the introduced jet plasma.

There has also been efforts to explore the magnetic field structure in clusters by analysing the power spectrum of RMs in clusters. Using both the measured power spectrum and the auto-correlation function of the RMs (which is related to the 2nd order structure function), the magnetic field power spectrum can be estimated (Vogt & Enßlin, 2005). To this point, this analysis has almost exclusively been performed on central radio sources (Enßlin & Vogt, 2003a; Vacca *et al.*, 2012, e.g.). These central sources, which can often span up to 100kpc in length, present the only suitable means in which to use this analysis. This is a result of these sources often encompassing many coherent RM patches within the ICM. Thus, it is possible to explore the entire inertial range of the power spectrum giving a complete view of the magnetic turbulence, If sources smaller with linear sizes smaller than one RM coherence length were probed, the power spectrum produced could potentially be missing information on the largest scales in the inertial range, which could lead to poor estimations of the magnetic field.
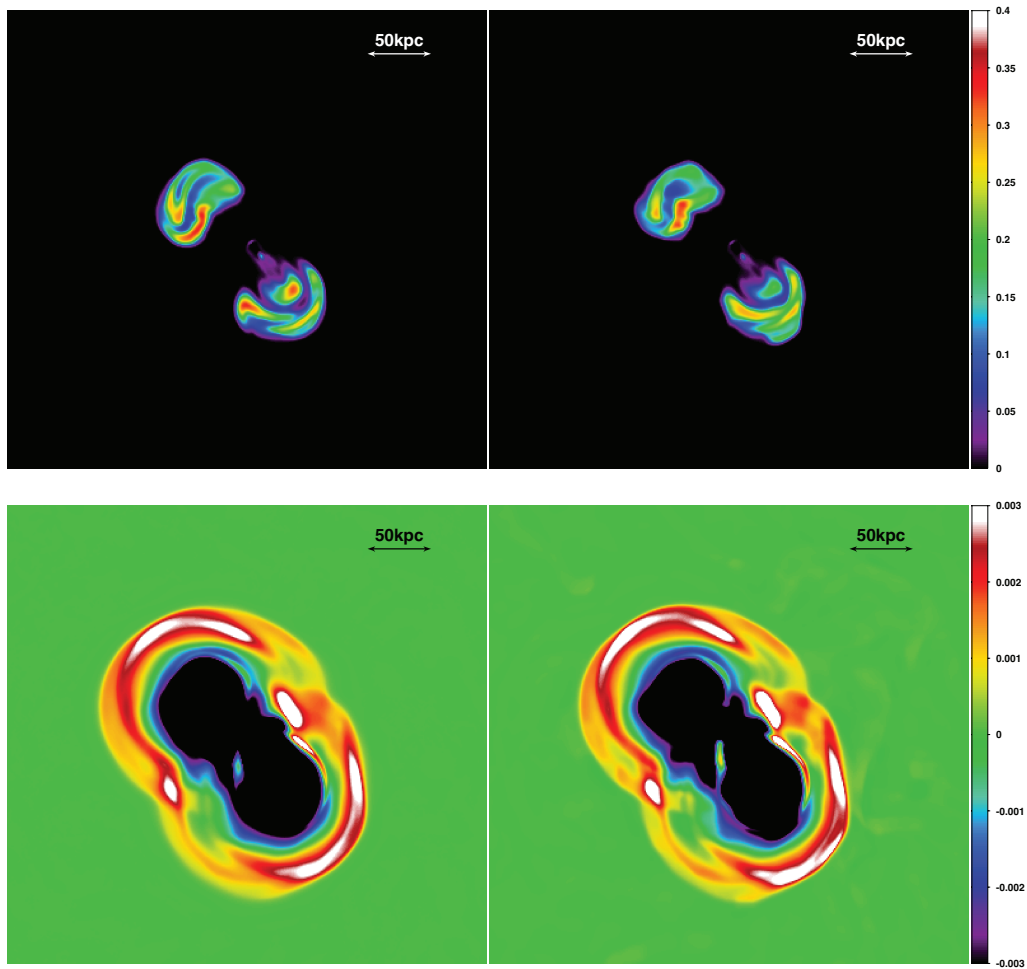
5.5   Figures

Figure 5.1 The fractional mass density (color) of the jet plasma relative to the ICM plasma (top) and difference in density between the AGN simulations and *NoAGN* for jet plasma $\beta = 100$ (left) and $\beta = 1$ (right). The density scale is in units of cm^{-3}. All figures were calculated in the same slice through the jet lobe region. The viewing angle is down the Z-axis.
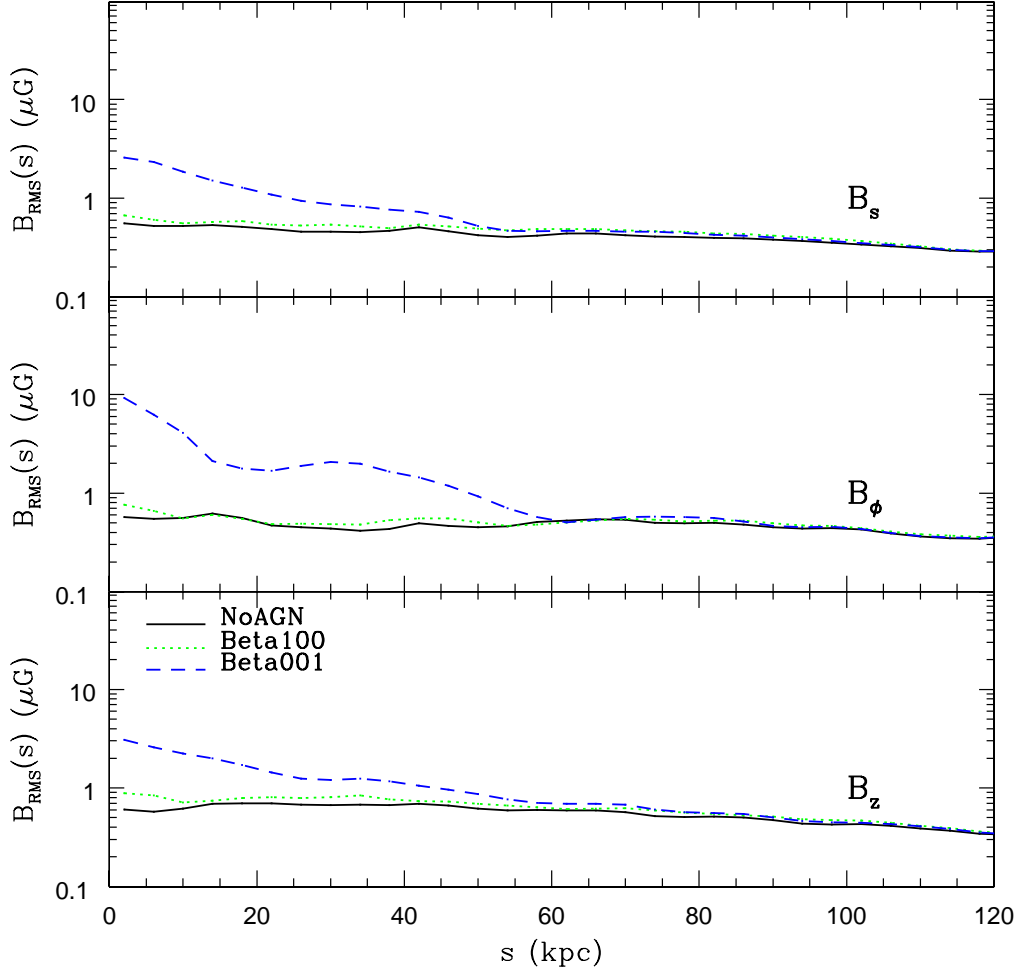
Figure 5.2 Dispersion of the three components of the magnetic field, calculated over concentric cylindrical shell of thickness $4kpc$, centered on the jet axis, and plotted as a function of cylinder radius, s. We show the results from both *Beta100* (dotted lines) and *Beta001* (dashed lines). The figure shows the components at the $t = 92$ Myrs epoch. The black lines correspond to the NoAGN run. The top panel corresponds to the $B_{\bar{s}}$ component of the field, middle panel to the $B_{\bar{\phi}}$ component of the field, and lower panel to the $B_{\bar{z}}$ component of the field.
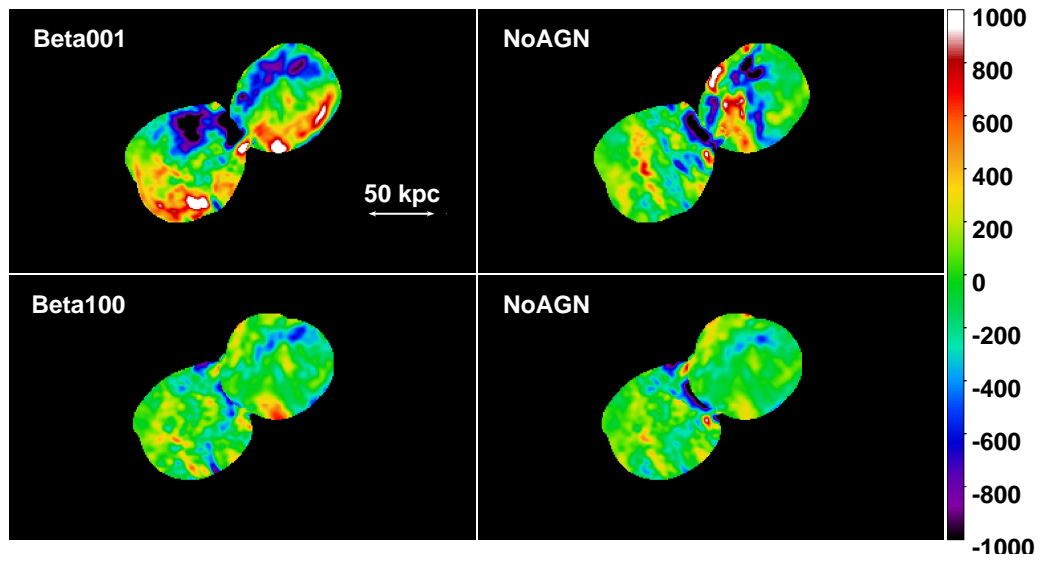
Figure 5.3 RM maps given a projection angle down the grid z-axis. The top-left panel displays the *Beta001* run with a full path screen. The top left panel displays *NoAGN* for a full path screen. The lower left panel displays *Beta100* for a foreground screen. The lower right panel displays *NoAGN* for a foreground screen. Units on the color bar are in $radm^{-2}$.
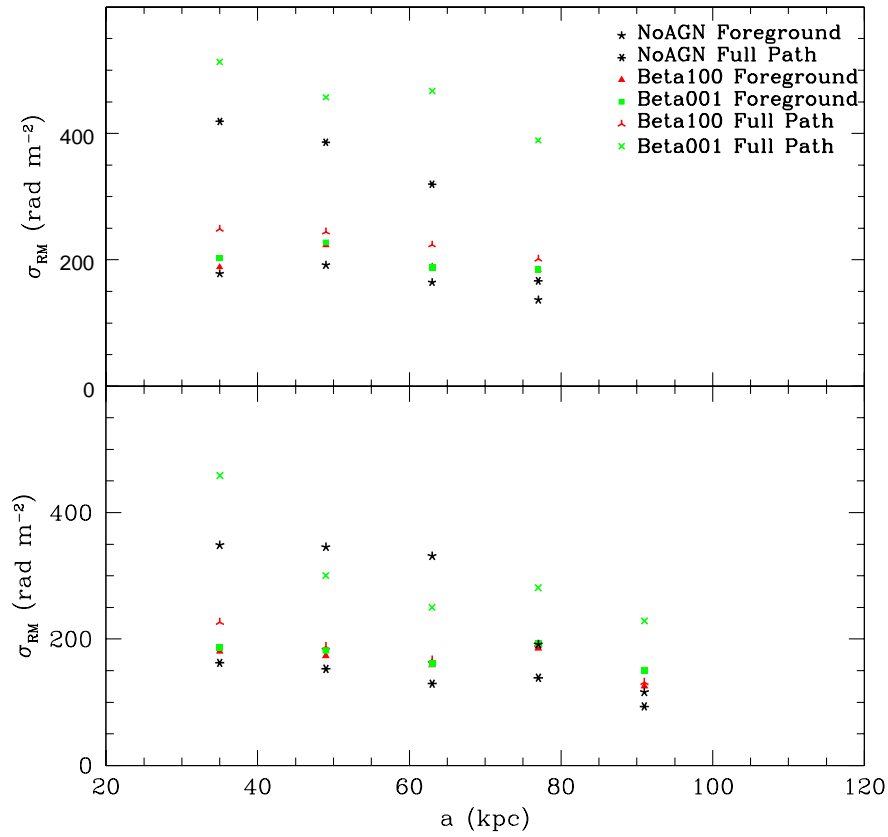
Figure 5.4 $\sigma_{RM}(a)$ profiles at $t = 80Myrs$ (top) and $t = 92Myrs$ (bottom). Both viewing angles are along the Z-axis. σ_{RM} values for each a were calculated by binning all RMs within a projected distance $a - 7kpc$ to $a + 7kpc$ an calculating σ_{RM} with each bin.

Table 5.1. $\sigma_{B,0}$ Statistics for an Interacting Central Radio Source

	$\langle\Lambda_0\rangle$	$\langle\sigma_{B,0.5}\rangle$	$range_1(\sigma_{B,0.5})$	$range_2(\sigma_{B,0.5})$	$\langle\sigma_{B,0.4}\rangle$	$range_1(\sigma_{B,0.4})$	$range_2(\sigma_{B,0.4})$
t = 80 Myrs							
Full Path *Beta100*	18	1.55	1.05-1.99	0.99-2.22	1.45	0.99-1.87	0.94-2.02
Full Path NoAGN 100-Screen	16	2.36	1.62-2.61	1.51-3.90	2.19	1.50-2.46	1.42-3.49
Full Path *Beta001*	38	2.53	1.91-3.58	1.64-3.81	2.36	1.81-3.26	1.56-3.44
Foreground *Beta100*	24	1.17	0.77-1.49	0.73-1.63	1.09	0.73-1.41	0.69-1.48
Foreground NoAGN 100-Screen	20	1.11	0.74-1.53	0.62-1.57	1.04	0.70-1.43	0.57-1.48
Foreground*Beta001*	19	1.51	1.07-2.04	0.84-2.14	1.41	1.02-1.91	0.79-1.94
t = 92 Myrs							
Full Path *Beta100*	20	1.32	0.89-1.53	0.77-1.87	1.22	0.72-1.68	0.72-1.68
Full Path NoAGN 100-Screen	15	2.20	1.40-2.45	1.39-3.73	2.02	1.30-2.29	1.29-3.28
Full Path *Beta001*	16	2.94	2.10-3.51	2.06-3.91	2.71	1.98-3.26	1.94-3.50
Foreground *Beta100*	21	1.11	0.64-1.38	0.63-1.53	1.03	0.60-1.3	0.59-1.37
Foreground NoAGN 100-Screen	23	1.04	0.64-1.35	0.61-1.74	0.96	0.60-1.20	0.54-1.62
Foreground*Beta001*	19	1.33	0.75-1.79	0.71-1.89	1.23	0.71-1.69	0.67-1.70

Note. — Statistical values of the estimated $\sigma_{B,0}$ value using RMs from an interacting radio source. Averages are calculated over all projected angles for a given experiment. Ranges incorporate only 6 of the 8 projected angles for each scenario, with the 2 extreme data points excluded. The values of σ_B are in μG and Λ_0 in kpc. The foreground screen and jet-axis experiments were calculated using the *NoAGN* simulation with masks obtained from the *Beta100* simulation. The numerical value in the subscript of σ_b corresponds to the fixed η value used, with "real" corresponding to the actual η value of the real magnetic field in the cluster. $range_1$ shows σ_B for only 6 of the 8 projected angles for each scenario, with the 2 extreme ata points excluded and approximates a $1 - \sigma$ spread in the data. $range_2$ shows the full range of $sigma_B$ for all 8 projected angles. Fitted values for the real 3D field in the cluster are t = 80 Myrs: $\sigma_{B,0} = 1.79, \eta = 0.41$; t = 92 Myrs: $\sigma_{B,0} = 1.60, \eta = 0.39$.

Chapter 6

Conclusion and Discussion

We have taken an idealized approach by using RMs to isolate uncertainties that may be present when estimating cluster magnetic fields. To keep our analysis as general as possible, we extract from a cosmological simulation a representative, morphologically relaxed cluster, that is still dynamically active. This allows us to look at a cluster containing magnetic fields that have dynamically evolved from primordial fields as well as possessing non-idealized motions such as large scale flows and other cluster "weather". We can then compare our estimates to the known magnetic field values in the cluster, and determine where these inherent sources of error arise.

We have assumed that the magnetic field scales as $B \sim n_e^{\eta}$ and that the field is turbulent with a characteristic coherence scaling. By the standard statistical model for σ_{RM}, this coherence scale is related to the characteristic length needed to estimate the magnetic field strengths in the cluster. It is suggested that this length not be directly associated with any physical properties of the cluster magnetic field, and thus attributing it to models such as a Kolmogorov or other power law type spectral model of the magnetic field is discouraged. Instead, we suggest a simplistic way to obtain this parameter using 2nd order structure functions calculated from the RMs within a cluster. Given our cluster setup, we find that assuming Λ is is proportional to density by $\Lambda \propto n^{-\frac{1}{2}\eta}$ provides better estimates to the magnetic field in comparison to treating Λ as a cluster-wide constant. We verify this by using fully sampled cluster RMs from both background and mid-plane polarized screens to try and recover the known magnetic field dispersion in the cluster. Thus it is suggested to consider a density dependent Λ

when trying to estimate cluster magnetic fields from RM analyses.

We explore various uncertainties and their relative contributions towards the magnetic field estimates. The largest uncertainties arise from cluster scale anisotropies. Given reasonable assumptions in clusters, these uncertainties will most likely, at best, lead to $\sim 50\%$ errors in magnetic field estimates under ideal conditions. This result is model-independent and larger errors can be produced by difficulties in constraining $\sigma_{RM,0}$. For our random source experiments, we find that errors resulting from line of sight position uncertainties are small as long as the mean line of sight source position over all sources is located at the cluster mid-plane. Furthermore, the amount of sources is not a limitation in being able to effectively estimate the magnetic field strength within a cluster.

By modeling jets from a central AGN we have explored how the radio source influences the local ICM and resulting RMs. We have shown that if the jet plasma contains weak fields, there is minimal RM contribution from the jet lobe and evacuated cavity. In contrast, based on the physics incorporated in our simulations, when magnetic fields introduced by the AGN outflow are strong, the observed RMs are dominated by an ICM/jet-plasma mixture within the cavities. For radio sources with this behavior, magnetic field estimates using RMs are not reflective of the cluster ICM fields and are more strongly tied to the properties of the introduced jet plasma.

By our central AGN simulations, RMs are only slightly increased beyond the evacuated cavity as the ICM gets compressed between the bow shock and the leading contact discontinuity. Other than from magnetic field contamination by the jet plasma, the ICM magnetic fields throughout the cluster are largely unaffected by the jet outflow. If the contamination in the jet cavity is small, then the only significant RMs produced will be from the ICM between the observer and the near edge of the cavity. In this case, the mean distance to the "source" of the RMs will be some distance infront of the mid-plane. In this scenario, the deviation of the sources RMs from the mid-plane value will be tied strongly to the width of the jet cavity. As the width of the jet cavity approaches the core radius of the cluster, the observed RMs from the central source can decrease by factors of ~ 2. Underestimates of the central magnetic field dispersion of

the same order should be expected.

References

Bonafede, A., Feretti, L., Murgia, M., et al. 2010, A&A, 513, A30

Bonafede, A., Vazza, F., Bruggen, M., Murgia, M., Govoni, F., Feretti, L., Giovannini, G., Ogrean, G., 2013, MNRAS, accepted

Carilli, C. L., & Taylor, G. B., 2002, ARA&A, 40, 319

Cavaliere A., Fusco-Femiano R., 1976, A&A, 49, 137

Cho, J., & Ryu, D. 2009, ApJ, 705, L90

Cho, J., Vishniac, E. T., Beresnyak, A., Lazarian, A. & Ryu, D., 2009, ApJ, 693, 1449

Dolag, K., Grasso, D., Springel, V., Tkachev, I., 2005, JCAP, 1, 9

Dolag, K., Bykov AM, Diaferio A. 2008. Space Science Reviews 134:311335

Dolag, K. & Stasyszyn, F. 2009, MNRAS, **398**, 1678

Dolag, K., Borgani, S., Murante, G. & Springel, V., 2009,MNRAS, 399, 497

Eilek, J. A., Owen F. N., 2002, ApJ, 567, 202

Enßlin T.A., Vogt C., 2003, A&A, 401, 835

Enßlin T.A., Vogt C., Clarke T.E., Taylor G.B., 2003, ApJ, 597, 870

Felten, J. E., 1996, Clusters, Lensing, and the Future of the Universe, ed. V. Trimble, & A. Reisenegger, ASP Conf. Ser., 88, 271

Feretti L., Dallacasa D., Govoni F., Giovannini G., Taylor G. B., Klein U., 1999, A&A, 344, 472

Govoni, F., Murgia, M., Feretti, L., et al. 2006, A&A, 460, 425

Guidetti, D., Laing R.A., Bridle A.H., Parma P., Gregorini L., 2011, MNRAS, **413**, 2525

Guidetti, D., Laing R.A., Croston J.H., Bridle A.H., Parma P., 2012, MNRAS, **423**, 1335

Huarte-Espinosa, M., Krause, M., & Alexander, P. 2011, MNRAS, **418**, 162

Jones, T. W., Porter, D. H., Ryu, D., & Cho, J. 2011, Mem. Soc. Astron. It., 82, 588

Kunz M., Schekochihin A., Cowley S., Binney J., Sanders J., 2011, MNRAS, **410**, 2446

Laing, R. A., Bridle, A. H., Parma, P., & Murgia, M., 2008, MNRAS, **391**, 521

Li, H., Lapenta, G., Finn, J. M., Li, S., & Colgate, S. A. 2006, ApJ, 643, 92

Mendygral, P. J., Jones, T. W., & Dolag, K., 2012, ApJ, 750, 166

Murgia M., Govoni F., Feretti L., et al., 2004, A&A 424, 429

O'Neill, S. M. & Jones, T. W., 2010, ApJ, 710, 180

Parrish I. J., McCourt M., Quataert E., Sharma P. 2012, MNRAS, **422**, 704

Rudnick, L. & Blundell, K. M., ApJ, 588, 143

Sanders, J.S., Fabian, A.C., & Smith, R.K. 2011, MNRAS, **410**, 1797

Schekochihin, A. A., Cowley, S. C., Taylor, S. F., Maron, J. L., & McWilliams, J. C. 2004, ApJ, 612, 276

Schuecker P., Finoguenov A., Miniati F., Bohringer H., Briel U. G., 2004, A&A, 426, 387

Taylor, G. B., Gugliucci, N. E., Fabian, A. C., Sanders, J. S., Gentile, G., & Allen, S. W. 2006, MNRAS, **368**, 1500

Taylor, G. B., & Perley, R. A. 1993, ApJ, 416, 554

Vacca, V., Murgia, M., Govoni, F., et al. 2012, A&A, 540, A38

Vikhlinin, A., Kravtsov, A., Forman, W., Jones, C., Markevitch, M., Murray, S. S., & Van Speybroeck, L. 2006, ApJ, 640, 691

Vogt, C., & Enßlin, T. A. 2005, A&A, 434, 67

Xu, H., Li, .H., Collins, D. C., Li, S. & Norman, M. L., 2011, ApJ, 739, 77

Xu, H., Govoni, F., Murgia, M., Li, H., Collins, D. C., Norman, M. L., Cen, R., Feretti, L., & Giovannini, G., 2012, ApJ, 759, 40

Zhuravleva, I., Chrurazov, E., Sazonov, S., Sunyaev, R. & Dolag, K., 2011, Ast. Lett., 37, 141

Zuhone, J. A., Markevitch, M. & Lee, D., 2010, ApJ, 743, 16